End-Bridging Monte Carlo: A Fast Algorithm for Atomistic Simulation of Condensed Phases of Long Polymer Chains

Vlasis G. Mavrantzas,[†,‡] Travis D. Boone,[§] Evangelia Zervopoulou,[†,||] and Doros N. Theodorou*[,†,‡,||]

Department of Chemical Engineering, University of Patras, GR 26500 Patras, Greece, Institute of Chemical Engineering and High Temperature Chemical Processes, GR 26500 Patras, Greece, Soane Technologies, Inc., 3961 Trust Way, Hayward, California 94545, and Molecular Modelling of Materials Laboratory, Institute of Physical Chemistry, National Research Centre for Physical Sciences "Demokritos", GR 15310 Ag. Paraskevi Attikis, Greece

Received November 9, 1998; Revised Manuscript Received April 9, 1999

ABSTRACT: The recently introduced end-bridging (EB) Monte Carlo move is revisited, and a thorough analysis of its geometric formulation and numerical implementation is given. Detailed results are presented from applying the move, along with concerted rotation, in atomistic simulations of polyethylene (PE) melt systems with mean molecular lengths ranging from C_{78} up to C_{500}, flat molecular weight distributions, and polydispersity indices I ranging from 1.02 to 1.12. To avoid finite system-size effects, most simulations are executed in a superbox containing up to 5000 mers and special neighbor list strategies are implemented. For all chain lengths considered, excellent equilibration is observed of the thermodynamic and conformational properties of the melt at all length scales, from the level of the bond length to the level of the chain end-to-end vector. In sharp contrast, if no end bridging is allowed among the Monte Carlo moves, no equilibration is achieved, even for the C_{78} system. The polydispersity index I is found to have no effect on the equilibrium properties of the melt. To quantify the efficiency of the EB Monte Carlo move, the CPU time t_0 required for the chain center of mass to travel a distance equal to the root-mean-square end-to-end distance is estimated by simple analytical arguments. It is found that t_0 should scale as $n/(\bar{X}\Delta^{2.5})$, where n is the total number of mers in the system, $\bar{X}$ is the average chain length, and $\Delta \simeq [3(I-1)]^{1/2}$ is the reduced width of the chain-length distribution function. This means that, if the size of the model system and the shape of the chain-length distribution are kept constant, systems of larger average molecular weight equilibrate faster, a remarkable attribute of the EB Monte Carlo method. The simulation results obey the estimated scaling of t_0 with $\bar{X}$, n, and Δ remarkably well in the range of chain lengths and polydispersities for which the premises of the analysis are not violated (mean chain lengths greater than C_{156} and polydispersity indices above about 1.07). Results for volumetric behavior, structure, and chain conformation at temperature $T = 450$ K and pressure P ranging from 1 to 800 atm are presented, using three different PE united atom models proposed in the recent literature. All three models are shown to overestimate the density by ca. 4% and also overestimate the stiffness of chains. The Yoon et al. model is in best agreement with experimental characteristic ratios. Simulation predictions for the structure factor and for the chain-length dependence of the density are in excellent agreement with experiment.

1. Introduction

The structural, thermodynamic, and dynamic properties of polymers in the liquid state play a central role in chemical technology (plastics manufacture, transportation, microelectronics, separation technology, performance of lubricants, and processing of foodstuffs) and also in macromolecular biology. Of particular importance among the properties of polymers is their viscoelastic rheological behavior, which governs their processability in the molten state. Viscoelasticity is a direct manifestation of the large length-scale (conformational) structure of polymer melts and constitutes their most distinctive feature in comparison with simple fluids. The reliable development of a methodology for the prediction of bulk and interfacial rheological properties of polymers requires a good understanding of their structure and dynamics over a wide spectrum of length scales, from the level of individual segments to the level of entire chains.

In the last years, in parallel to theoretical works,[1−4] molecular simulation techniques (molecular dynamics (MD) and Monte Carlo (MC)) have offered a promising avenue for predicting structural, conformational, thermodynamic, and dynamic properties from the chemical constitution of chains,[5−12] while simultaneously avoiding many of the assumptions invoked in the analysis of the theoretical models. Weber and Helfand[13] were the first to present an atomistic MD simulation of a liquid polyethylene (PE) model with no chain ends. Later, extensive MD studies of short-chain PE were undertaken by Rigby and Roe.[14] Vacatello et al.[15] reported the first MC simulation of liquid C_{30} in continuous space. Theodorou and Suter[16] developed a molecular mechanics (MM) method for the detailed atomistic simulation of a vinyl polymer glass (atactic polypropylene) and of its mechanical properties. Building on these earlier works, a considerable number of MD, MC, and MM simulations were carried out in the ensuing years, which broadened our knowledge of structure−property relations in polymer melts and glasses[17−20] and also permitted the atomistic modeling of condensed phases of chain molecules with more complex chemical constitution than the polyolefins.[21]

* Author to whom correspondence should be addressed at the University of Patras. Phone: +3061-997-398. Fax: +3061-993-255. E-mail: doros@sequoia.chemeng.upatras.gr.
[†] University of Patras.
[‡] Institute of Chemical Engineering and High Temperature Chemical Processes.
[§] Soane Technologies, Inc.
[||] National Research Centre for Physical Sciences "Demokritos".

10.1021/ma981745g CCC: $18.00
Published on Web 07/10/1999

With very few exceptions, most simulation work has been limited to polymer systems composed of relatively short chains. For MD simulations, in particular, this limitation is due to a natural constraint, namely, the fast increase of the longest relaxation time with increasing chain length;[22,23] even for relatively short-chain melts (e.g., linear C_{150}) the longest relaxation time considerably exceeds the time spans (a few tens of nanoseconds) that can be simulated with reasonable contemporary supercomputer resources. Obviously, this strong limitation renders the full equilibration of entangled, truly polymeric systems impossible by brute-force MD. A few examples are quite characteristic of the situation: the longest relaxation time of a C_{44} melt is about 0.35 ns, of a C_{70} about 2.3 ns, of a C_{140} about 20 ns, of a C_{212} about 75 ns, of a C_{283} about 160 ns, and of a C_{812} about 3350 ns.[24] This is the main reason why MD simulations have for a long time been restricted to short-chain systems, of length up to C_{40}, and it is only very recently and with the power of the newest supercomputer systems that the simulation of longer-chain melts, such as C_{100}, has become possible.[25]

In an MD simulation of a long-chain polymer, the large-scale conformational characteristics of the system are given too little time to evolve, and the system will mostly remain trapped within the neighborhood of the initial configuration. This results in insufficient sampling of the configuration space and unreliable estimation of the dynamic and structural properties of the melt in the terminal region, which is the region of relevance to rheological applications.

From the point of view of applications, the ability to reliably predict the constitutive laws and property values describing the viscoelastic response of long-chain polymers to deformation from the chemical structure of their constituent chains is of paramount importance for almost all polymer processing operations. The sharp decrease in self-diffusion coefficient, the large increase in viscosity, and the rubberlike plateau in the relaxation modulus exhibited by polymer melts when their molecular weight (MW) is increased above a critical value[3] (the entanglement MW) all constitute fundamental issues in polymer science and at the same time determine the upper limits of production rates in technological applications. The need for a better understanding of the structural, configurational, and dynamic properties of polymeric materials as a function of MW, particularly when this approaches and/or exceeds the entanglement value, has motivated considerable theoretical and computational efforts in recent years.

Despite its inability to effectively sample the configurational space of large, dense systems and track their long-time and large-length-scale behavior, MD has continued to be the dominant method in the area of computer simulation of polymers, primarily because of its inherent dynamical nature and unique capability to give real-time information about the system evolution. No other technique can provide such quality of information about system dynamics. If one is interested in the static (thermodynamic) properties of the system, however, MC offers an excellent alternative for the simulation of dense polymer melts through the design of clever moves tailored to enhance the vigor and efficiency of configurational sampling and thus accelerate the equilibration of the system. Because there is no limit on how clever such a new move can be, MC techniques do not suffer from the limitations encountered in MD simulations. More importantly, MC techniques offer the opportunity of subjecting the system that has already been relaxed by MC to an MD study, which can help to extend the simulation time to longer scales.

Over the last few years, several MC moves specific to chain molecules have been developed and employed in molecular simulations in continuous space, the most successful being the reptation (REPT), the configurational bias (CB), and the concerted rotation (CONROT) moves. In the reptation move, first introduced by Vacatello et al.[15] for the simulation of liquid C_{30} and later used by Boyd[20] for the modeling of liquid C_{24}, an end segment of a randomly selected chain is initially cut off and then appended to the other end with a randomly selected torsion angle. In the configurational bias method,[26−28] a randomly selected chain is cut at a random point to form two subchains. One of these subchains is removed from the system and subsequently regrown, segment by segment, in a biased fashion, which avoids overlaps with the surrounding segments in the same or in neighboring chains. The bias introduced by this selective construction is removed from the system with proper modification of the acceptance criteria.

The concerted rotation (CONROT) move, first presented by Dodd et al.[29] and later generalized by Pant and Theodorou,[30] was introduced in order to effect significant local rearrangements also to the interior of the chains (and not only to the ends). The move is initiated by excising a randomly selected internal trimer of skeletal atoms in the polymer. In the original formulation[29] (unidirectional CONROT), one atom neighboring the trimer is displaced by changing its "driver" torsion angle by an amount randomly selected within prespecified bounds ($-\delta\phi_{max}$, $\delta\phi_{max}$), and the trimer is then reconstructed. In the more general formulation[30] (termed intramolecular rebridging move or double-driven CONROT), both atoms neighboring the excised trimer are displaced by imposing randomly selected changes to both torsion angles neighboring the trimer on its two sides, thus removing any directionality from the move; the trimer is then reconstructed. In the symmetric version of CONROT, which we will focus on in the following, a total of five skeletal segments are ultimately relocated and eight torsion angles are altered.

The very efficient CB and CONROT moves have permitted complete equilibration over all length scales for polymer melts with chain length up to C_{30}. For longer-chain systems (for example, C_{70}), however, it is generally observed that, although these moves do reliably sample local density and energy fluctuations, they are not sufficient for equilibrating the conformational characteristics of chains at larger length scales, for example, at the level of the end-to-end distance. Within the limits of reasonable CPU times, important descriptors such as the orientation of the end-to-end distance vector or the orientation of the principal axes of the chain segment cloud do not completely "forget" the values they had at the beginning of the simulation.[31] This problem, which, as stated above, also shows up in MD simulations, precludes the reliable estimation of the viscoelastic properties of long polymers that depend strongly on the large-scale features of the chains.

A solution to the problem of efficient sampling of the large-length-scale characteristics of long polymer chains was presented by Pant and Theodorou,[30] who introduced

the end-bridging (EB) Monte Carlo move. This connectivity-altering move greatly enhances the efficiency with which widely different molecular configurations are sampled. During such an EB move, two melt chains are selected so that the end of one is within a certain bridging distance from a backbone segment of the other. A trimer centered at this latter backbone segment is excised from the second chain, thus defining two subchains. The end of one of these subchains is connected to the end of the first chain by constructing a bridging trimer, forming a new chain with prescribed molecular geometry (bond lengths and bond angles). The selection of the chains, the building of the bridging trimer, and the acceptance criteria of the method are designed so that the requirements of microscopic reversibility for proper sampling are satisfied.

Clearly, the EB move alters the lengths of the chains participating in it. To control the chain length distribution at equilibrium, Pant and Theodorou[30] cast this move in a semi-grand canonical ensemble formalism. In the new ensemble, the following parameters are held fixed: the pressure P, the temperature T, the total number of chains N, the total number of mers n, and the relative chemical potentials μ_k^* of all chain species in the system except two, which are taken as reference species. In this $NnPT\boldsymbol{\mu}^*$ ensemble, the molecular weight distribution of the system is completely defined by appropriately specifying the distribution of the relative chemical potentials. Within this formulation, for the first time, the EB move has not only permitted the study of longer chain systems but also opened up the way to atomistic modeling of polydisperse melts with fully controlled MW distribution.

Pant and Theodorou[30] derived and fully tested expressions for the spectrum of relative chemical potentials that faithfully reproduce the most widely encountered limiting molecular weight distributions. They also employed the new method in a MC simulation of the C_{78} polymer melt for which previous results about structural and volumetric properties were readily available. Simulation estimates compared very favorably with experiment, and excellent agreement with Flory's random coil hypothesis[32] for chain conformations was established.

Despite their rigorous presentation of the statistical mechanics fundamentals of the end-bridging move (formulation, incorporation of appropriate Jacobians of transformations in the acceptance criteria, correct accounting of the multiplicity of solutions, and proper handling of polydispersity), Pant and Theodorou[30] did not give details on the geometric implementation of the new move. They also did not quantify the efficiency of the move in full detail: their investigation was restricted to demonstrating equilibration and comparing results with those from previous works. Thus, significant issues such as the relationship between the simulation efficiency of the new method and the average chain length or width of the chain-length distribution function, the performance of the new move on significantly longer chain systems, and the computational requirements of the EB Monte Carlo method in relation to MD and other MC methods were left unanswered. It is the purpose of this paper to address these issues by presenting (a) a new formulation of the geometric problem of trimer bridging involved in EB and CONROT, which simplifies the problem and facilitates its solution, (b) a computationally efficient numerical implementation of this formulation, and (c) results from applying EB Monte Carlo to polymer melt systems of average chain length significantly larger than what has been simulated up to now. Through these studies, we will (a) demonstrate the superiority of the end-bridging move over all other simulation methods available in the literature for equilibrating long-chain polymer melts with prespecified MW distribution, (b) present quantitative results on the performance of the method and its scaling with the average chain length, the width of the chain-length distribution function, and the size of the model system, and (c) discuss our simulation findings for the conformational, volumetric, and structural properties of several linear PE melts of mean chain length ranging from C_{78} up to C_{500}.

The next section presents a short discussion of the molecular model adopted in the present investigation. Section 3 presents a new, complete geometric formulation of the trimer bridging problem involved in EB and CONROT moves, a numerical solution procedure associated with this formulation, and the correct MC attempt and acceptance probabilities associated with the EB move. Section 4 presents the simulation strategy and the most important features of the algorithm used to implement the EB Monte Carlo method. Section 5 presents results on the CPU time requirements of EB, how they scale with model system parameters, and how they compare to those of other methods. Section 5 also reports new data on the conformational, volumetric, and structural properties of various model systems of linear PE with average length varying between C_{78} and C_{500}. Section 6 presents the conclusions and a summary of the most important points of the work.

2. Molecular Model

Most calculations reported here have been performed with the model used in our previous studies of elasticity and viscosity of linear PE melts,[33,34] which will be referred to as "this model". In this model, the united-atom description is adopted, with each methyl and methylene group along the chain regarded as an interacting site. For intramolecular interactions between sites separated by more than three bonds along the chain and for all intermolecular interactions, a Lennard-Jones (LJ) potential is used with a diameter $\sigma = 3.94$ Å and a well depth $\epsilon = 0.098$ kcal/mol. Bond lengths are kept constant at their average value of 1.54 Å, whereas bond angles are assumed to fluctuate around an equilibrium angle of 112° subject to the Van der Ploeg and Berendsen[35] bending potential. All dihedral angles are governed by the torsional potential of Ryckaert and Bellemans.[36] The simulations are performed in a cubic box filled with chain segments and characterized by periodic boundary conditions in all three directions.

Because the primary objective of the work is to evaluate the efficiency of the new simulation technique and its superiority to other MC schemes, the issue of refining potential parameters both for the nonbonded interactions (through, for example, the use of anisotropic united atoms) and for the torsional potential (through the use of other functional forms) was not considered here. However, in order to have a feeling of the effects of the molecular model on the thermodynamic and (mainly) conformational properties of the system, a number of simulations have also been executed for the shorter chain systems studied here, the C_{78} and a C_{24} PE melt, with two other molecular models widely used in the literature. The first has been introduced by Smit et al.[37] to calculate the vapor−liquid equilibria of several

Table 1. Atomistic Molecular Models for *n*-Alkanes

	potential function and parameters		
type of interaction	this model[33]	Smit et al. model[37]	Yoon et al. model[38]
nonbonded interactions		$V_{LJ}(r_{ij}) = 4\epsilon\left[\left(\frac{\sigma_{ij}}{r_{ij}}\right)^{12} - \left(\frac{\sigma_{ij}}{r_{ij}}\right)^{6}\right]$	
	$\frac{\epsilon_{CH_3}}{k_B} = \frac{\epsilon_{CH_2}}{k_B} = 49.3$ K $\sigma_{CH_3} = \sigma_{CH_2} = 3.94$ Å	$\frac{\epsilon_{CH_3}}{k_B} = 114$ K $\frac{\epsilon_{CH_2}}{k_B} = 47$ K $\sigma_{CH_3} = \sigma_{CH_2} = 3.93$ Å	$\frac{\epsilon_{CH_3}}{k_B} = 113.96$ K $\frac{\epsilon_{CH_2}}{k_B} = 47.03$ K $\sigma_{CH_3} = \sigma_{CH_2} = 4.009$ Å
bond lengths	constrained $l = 1.54$ Å	constrained $l = 1.54$ Å	constrained $l = 1.53$ Å
bond bending	$\frac{V_{bend}(\theta)}{k_B} = \frac{1}{2}k_\theta(\theta - \theta_0)^2$ $k_\theta = 57\,950$ K rad^{-2} $\theta_0 = 112°$	$\frac{V_{bend}(\theta)}{k_B} = \frac{1}{2}k_\theta(\theta - \theta_0)^2$ $k_\theta = 62\,500$ K rad^{-2} $\theta_0 = 114°$	$\frac{V_{bend}(\theta)}{k_B} = \frac{1}{2}k_\theta(\cos(\theta) - \cos(\theta_0))^2$ $k_\theta = 60\,380$ K rad^{-2} $\theta_0 = 110°$
dihedral angles	$\frac{V_{tor}(\phi)}{k_B} = \sum_{k=0}^{5} c_k \cos^k(\phi)$ $c_0 = 1116$ K, $c_1 = 1462$ K, $c_2 = -1578$ K, $c_3 = -368$ K, $c_4 = 3156$ K, $c_5 = -3788$ K	$\frac{V_{tor}(\phi)}{k_B} = c_1(1 + \cos\phi) + c_2(1 - \cos(2\phi)) + c_3(1 + \cos(3\phi))$ $c_1 = 355.03$ K, $c_2 = -68.19$ K, $c_3 = 791.32$ K	$\frac{V_{tor}(\phi)}{k_B} = \frac{1}{2}[k_\phi{}^1(1 - \cos\phi) + k_\phi{}^2(1 - \cos(2\phi)) + k_\phi{}^3(1 - \cos(3\phi)]$ $k_\phi{}^1 = 754.91$ K, $k_\phi{}^2 = -384.5$ K, $k_\phi{}^3 = 1761.45$ K

normal alkanes near their critical points and will be referred to in the following as the "Smit et al." model. The second was introduced by Yoon and collaborators[38] in their MD simulation of linear PE melts and will be referred to as the "Yoon et al." model in the following. The three models differ primarily in the form of the torsional potential used; also, the Smit et al. and Yoon et al. models differentiate between end methyls and internal methylene groups. The Smit et al. model is believed to reproduce more reliably the thermodynamic (*PVT*) properties, whereas the Yoon et al. model is believed to reproduce more accurately the conformational properties of long polymers. Note that the "modified torsional potential" of ref 38 is used in this work. The detailed form of the potentials used in all three of these models is shown in Table 1. The torsion angle ϕ in the trans state is taken as zero in this model and the Yoon et al. model and as π in the Smit et al. model.

3. End-Bridging Monte Carlo Move

3.1. Fundamentals. The EB and the CONROT (intramolecular rebridging) moves admit a common mathematical formulation, for they address the same geometric problem: *Given two dimers in space, connect them with a trimer, such that the resulting heptamer has prescribed bond lengths and angles*. In the following we will refer to this problem as the *geometric problem of trimer bridging*. As noted by Pant and Theodorou,[30] infinite solutions to this problem are possible under special geometric conditions allowing the trimer to rotate freely without distorting the bonds and bond angles that connect it to the rest of the chain. Such "crankshaft" geometries, however, are precluded by the values of bond lengths and bond angles used in common molecular models, e.g., in the PE models described in section 2.

In CONROT it is possible to force microscopic reversibility by finding only one solution to the bridging problem.[30] Such a solution can be determined through an iterative Newton−Raphson procedure, with the initial trimer configuration serving as a convenient guess with which to start the iterations. If a geometrically viable solution is found, a solution of the reverse move is attempted through an identical Newton−Raphson procedure. By this scheme, microscopic reversibility is explicitly forced by rejecting all moves for which the reverse does not recreate the original configuration. A similar scheme cannot be attempted for the EB move, because of the lack of a convenient initial guess from which to start the Newton−Raphson iterations. Therefore, a different strategy is adopted, which involves the determination of all solutions to both the forward and the inverse bridging problems, and this is described in the present section. Because both EB and CONROT involve the same geometric problem of trimer bridging, this more general strategy is implemented for both moves.

3.2. Geometric Problem of Trimer Bridging. Throughout this formulation, Flory's local coordinate system[1] is employed, in which bond i connects skeletal atoms $i - 1$ and i and the dihedral angle for bond i is denoted by ϕ_i, the supplement of the skeletal bond angle with apex at atom i by θ_i, and the length of bond i by l_i.

The geometric problem to be analyzed is depicted in Figure 1, which illustrates schematically the EB move. In the end-bridging move (Figure 1) p is the attacking end of chain 1 and (k, l, m) is the trimer to be excised from the victim chain 2. The attacking end p is bridged to internal segment j of the victim chain; (k', l', m') is the trimer whereby this bridging is implemented. The two new chains resulting from the end-bridging move are labeled 1′ and 2′. Notice that the augmented attacking chain and the remnant of the victim chain retain their identity in the labeling.

In the CONROT move (see Figure 3 of ref 30), first, a trimer (k, l, m) is excised from a random position along the chain backbone. Next, the backbone atoms j and n neighboring the trimer are displaced to positions j' and n', respectively, by imposing independent random changes in the corresponding "driver" torsion angles. Finally, atoms j' and n' are "rebridged" with specified bond lengths and bond angles; trimer (k', l', m') now has a new position and orientation.

In both the CONROT and EB moves, the "rebridging" is attempted with specified bond lengths and bond angles. Furthermore, in the case of a fully explicit-atom description in the molecular model, or for branched polymers, all pendant atoms connected to k, l, m, j, and p or n, for an EB or a CONROT move, respectively, should be appropriately displaced in order to preserve the local intrachain geometry.

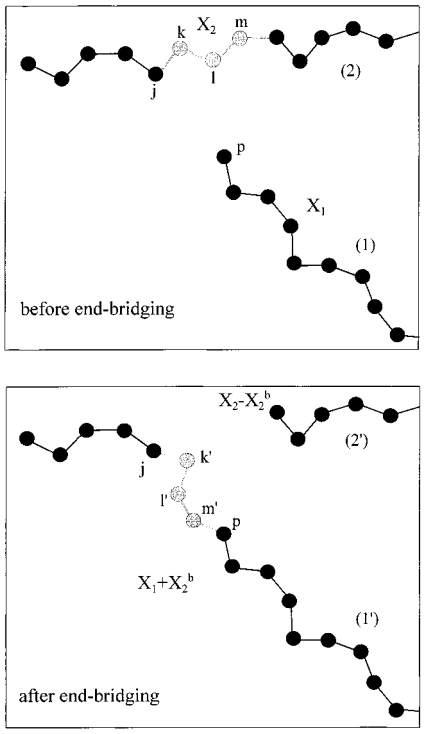

Figure 1. Schematic of the intermolecular end-bridging (EB) problem. Dark atoms are stationary, and lightly shaded atoms are mobile. Pendant groups are omitted for clarity. Top: Local configuration of the two chains prior to the EB move. The attacking chain is denoted as 1 and the victim chain as 2. Bottom: Trimer (k, l, m) of the victim chain is excised and end p of the attacking chain is bridged to internal mer j of the victim chain. Trimer (k', l', m') is the bridging trimer. The two new chains are labeled 1′ and 2′, respectively.

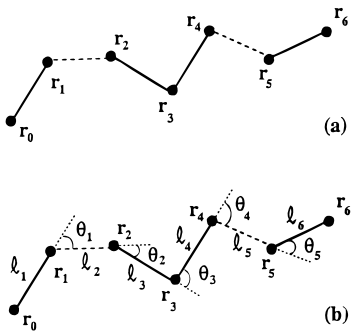

Figure 2. Bridging of two dimers with a trimer. (a) Trimer ($\mathbf{r}_2$, $\mathbf{r}_3$, $\mathbf{r}_4$) which bridges dimers ($\mathbf{r}_0$, $\mathbf{r}_1$) and ($\mathbf{r}_5$, $\mathbf{r}_6$). (b) Bond lengths and bond angles that are specified in the bridging construction.

Geometrically, the general problem of constructing a bridging trimer can be formulated by considering Figure 2. Given the two dimers ($\mathbf{r}_0$, $\mathbf{r}_1$) and ($\mathbf{r}_5$, $\mathbf{r}_6$) in space, the goal is to join them by a trimer ($\mathbf{r}_2$, $\mathbf{r}_3$, $\mathbf{r}_4$), such that the bond lengths (l_2, l_3, l_4, and l_5) and bond angles (θ_1, θ_2, θ_3, θ_4, and θ_5) have specified values.

Nine degrees of freedom are required to specify the position and orientation of the bridging trimer. These degrees of freedom can be chosen in various ways: e.g., in Cartesian coordinates, as the nine components of the three trimer atom positions ($\mathbf{r}_2$, $\mathbf{r}_3$, $\mathbf{r}_4$); in generalized coordinates of the trimer, as the three components of its first atom position ($\mathbf{r}_2$), three Eulerian angles describing the trimer orientation, two bond lengths (l_3 and l_4), and one bond angle (θ_3) describing its internal configuration; or in generalized coordinates of the whole chain, as (l_2, l_3, l_4, l_5, θ_1, θ_2, θ_3, θ_4, and θ_5). Regardless of the definition employed, the selected degrees of freedom can be reduced to 6 by specifying the two bond lengths (l_3 and l_4) and one bond angle (θ_3) that determine the internal geometry of the trimer. In this way, the problem can be cast as six equations in six unknowns, as in the original CONROT formulation.[29] The constraints requiring constancy of the internal degrees of freedom of the trimer will be referred to as $\mathbf{f}_{\text{trimer}} = (l_3, l_4, \theta_3)$.

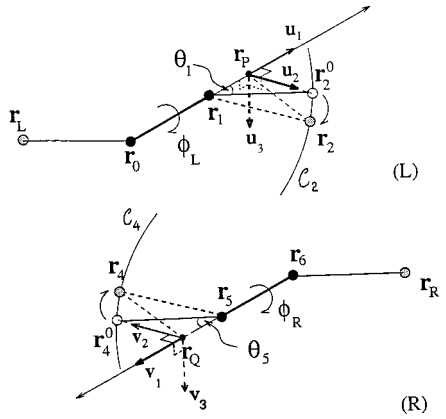

Figure 3. Frames of reference for the left- (L) and right-hand (R) sides of the trimer bridging problem. The position $\mathbf{r}_2$ is expressed in frame [$\mathbf{u}_1$, $\mathbf{u}_2$, $\mathbf{u}_3$] with origin $\mathbf{r}_P$. The position $\mathbf{r}_4$ is expressed in frame [$\mathbf{v}_1$, $\mathbf{v}_2$, $\mathbf{v}_3$] with origin $\mathbf{r}_Q$. Angles θ_1 and θ_5 are the bond angle supplements at vertices $\mathbf{r}_1$ and $\mathbf{r}_5$, respectively. All solid straight lines in the figure are coplanar.

The six remaining constraints that must be satisfied in bridging the two dimers are cast here as equations in the trimer Cartesian coordinates. Given the dimer positions ($\mathbf{r}_0$, $\mathbf{r}_1$) and ($\mathbf{r}_5$, $\mathbf{r}_6$), the bridging trimer configuration ($\mathbf{r}_2$, $\mathbf{r}_3$, $\mathbf{r}_4$) must be determined such that the bond lengths (l_2 and l_5) and bond angles (θ_1, θ_2, θ_4, and θ_5) or, equivalently (given $\mathbf{f}_{\text{trimer}}$), the bond lengths ($l_2$ and l_5), the bond angles (θ_1 and θ_5), and the interatomic distances (l_{13} and l_{53}), with $l_{ij} = |\mathbf{r}_j - \mathbf{r}_i|$, are held to specified values. These six bridging constraints will be referred to as $\mathbf{f}_{\text{bridging}} = (l_2, \theta_1, l_5, \theta_5, l_{13}, l_{53})$.

The trimer bridging problem can further be reduced to a problem of three equations in three unknown angular degrees of freedom. Our strategy for doing this rests on identifying three loci for the points $\mathbf{r}_2$, $\mathbf{r}_3$, and $\mathbf{r}_4$ which express the constraints $\mathbf{f}_{\text{bridging}}$, with the exact position of each point on its locus being described by one angular variable. With $\mathbf{r}_0$ and $\mathbf{r}_1$ fixed in space and l_2 and θ_1 specified, the locus of $\mathbf{r}_2$ is a circle C_2 lying in a plane normal to the line connecting $\mathbf{r}_0$ and $\mathbf{r}_1$, with its center on that line. Similarly, with $\mathbf{r}_5$ and $\mathbf{r}_6$ fixed in space and l_5 and θ_5 specified, the locus of $\mathbf{r}_4$ is a circle C_4 lying in a plane normal to the line connecting $\mathbf{r}_6$ and $\mathbf{r}_5$, with its center on that line (see Figure 3). To describe the positions of $\mathbf{r}_2$ and $\mathbf{r}_4$ along C_2 and C_4, respectively, it is convenient to introduce two fixed reference points, $\mathbf{r}_L$ and $\mathbf{r}_R$, as shown in Figure 3. With the introduction of the first reference point, $\mathbf{r}_L$, the rotation angle ϕ_L is defined as the dihedral angle between planes ($\mathbf{r}_L$, $\mathbf{r}_0$, $\mathbf{r}_1$) and ($\mathbf{r}_0$, $\mathbf{r}_1$, $\mathbf{r}_2$) (Figure 4L). The angle ϕ_L is taken as zero when $\mathbf{r}_L$ and $\mathbf{r}_2$ are in a "trans" configuration relative to $\mathbf{r}_1$ and $\mathbf{r}_2$ and its sign is defined following the Flory convention for torsion angles.[1] Similarly, with the introduction of the second reference point, $\mathbf{r}_R$, the rotation angle ϕ_R is defined as the dihedral angle between planes ($\mathbf{r}_5$, $\mathbf{r}_6$, $\mathbf{r}_R$) and ($\mathbf{r}_4$, $\mathbf{r}_5$, $\mathbf{r}_6$) (Figure 4R).

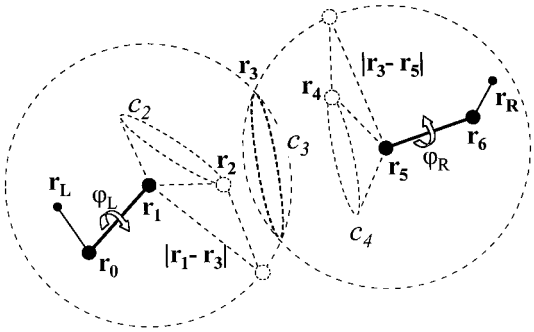

Figure 4. Schematic of the trimer bridging geometric solution. Shaded atoms are stationary. Fixed, but otherwise arbitrary, reference positions $\mathbf{r}_L$ and $\mathbf{r}_R$ are used to define torsion angles ϕ_L and ϕ_R on the left (L) and right (R) sides of the bridge, respectively. Rotations of ϕ_L and ϕ_R sweep out the loci of $\mathbf{r}_2$ and $\mathbf{r}_4$ (short dashed circles C_2 and C_4), respectively. The lengths of segments ($\mathbf{r}_1$, $\mathbf{r}_3$) and ($\mathbf{r}_3$, $\mathbf{r}_5$) constitute the radii (long dashed lines) of spheres centered at $\mathbf{r}_1$ and $\mathbf{r}_5$, respectively; these segment lengths are known from the chain bonding geometry. Position $\mathbf{r}_3$ must lie on the intersection (heavy dashed circle C_3) of these two spheres. Points $\mathbf{r}_2$, $\mathbf{r}_3$, and $\mathbf{r}_4$ on C_2, C_3, and C_4 which satisfy constraints $\mathbf{f}_{\text{trimer}}$ define solutions to the EB problem.

By varying the dihedral angles ϕ_L and ϕ_R, one causes $\mathbf{r}_2$ and $\mathbf{r}_4$ to sweep out their loci C_2 and C_4, respectively.

The reference positions $\mathbf{r}_L$ and $\mathbf{r}_R$ can be chosen in many ways. One possibility is to take $\mathbf{r}_L = \mathbf{r}_{-1}$ and $\mathbf{r}_R = \mathbf{r}_7$ (positions of skeletal atoms preceding $\mathbf{r}_0$ and following $\mathbf{r}_6$ along the chain), in which case $\phi_L = \phi_1$ and $\phi_R = \phi_6$, i.e., torsion angles along a local section of the chain backbone. Another possibility is to choose $\mathbf{r}_L = \mathbf{r}_5$ or $\mathbf{r}_6$ and $\mathbf{r}_R = \mathbf{r}_0$ or $\mathbf{r}_1$. With such a choice, the trimer bridging problem is completed using points $\mathbf{r}_0$, $\mathbf{r}_1$, $\mathbf{r}_5$, and $\mathbf{r}_6$ as the only fixed points. If the torsion angles describing the chain configuration are tracked throughout the MC simulation, the first choice enhances computational efficiency, and it is the one adopted here.

A locus for $\mathbf{r}_3$ is determined as follows: For fixed l_{13} (compare constraints $\mathbf{f}_{\text{bridging}}$ above), $\mathbf{r}_3$ lies on the surface of a sphere of radius l_{13} centered at $\mathbf{r}_1$. Similarly, for fixed l_{53}, $\mathbf{r}_3$ lies on the surface of a sphere of radius l_{53} centered at $\mathbf{r}_5$. Therefore, $\mathbf{r}_3$ belongs to the intersection of two known spheres, i.e., on a circle C_3 with its center on the line connecting $\mathbf{r}_1$ and $\mathbf{r}_5$ (heavy dashed line in Figure 4). The exact position of $\mathbf{r}_3$ on C_3 is determined by one angular variable. Here, this is chosen as the dihedral angle ψ between planes ($\mathbf{r}_3$, $\mathbf{r}_1$, $\mathbf{r}_5$) and ($\mathbf{r}_M$, $\mathbf{r}_1$, $\mathbf{r}_5$) with $\mathbf{r}_M = (\mathbf{r}_0 + \mathbf{r}_6)/2$ (see Figure 5). Requiring that $\mathbf{r}_2$, $\mathbf{r}_3$, and $\mathbf{r}_4$ lie on C_2, C_3, and C_4, respectively, amounts to an elimination of the six constraints $\mathbf{f}_{\text{bridging}}$ from the nine equations in nine unknowns describing the trimer bridging problem. The three constraints $\mathbf{f}_{\text{trimer}}$ remain, however, and must be used to determine ϕ_L, ϕ_R, and ψ at the solution. Thus, the trimer bridging problem is reduced to the following general geometric problem: *Given three circles, C_2, C_3, and C_4 in space, determine one point on each circle ($\mathbf{r}_2 \in C_2$, $\mathbf{r}_3 \in C_3$, and $\mathbf{r}_4 \in C_4$), such that the distances $|\mathbf{r}_3 - \mathbf{r}_2|$, $|\mathbf{r}_4 - \mathbf{r}_3|$, and $|\mathbf{r}_2 - \mathbf{r}_4|$ between the three points have prespecified values (l_3,l_4, and $\sqrt{l_3^2+l_4^2+2l_3l_4\cos\theta_3}$, respectively.)*

Analytical expressions for $\mathbf{r}_2(\phi_L)$, $\mathbf{r}_3(\psi)$, and $\mathbf{r}_4(\phi_4)$ can be developed through the introduction of appropriate local coordinate frames, as described in detail in Appendix A. Substitution of these expressions into the three bond length and bond angle constraints $\mathbf{f}_{\text{trimer}}$ yields equations of the form

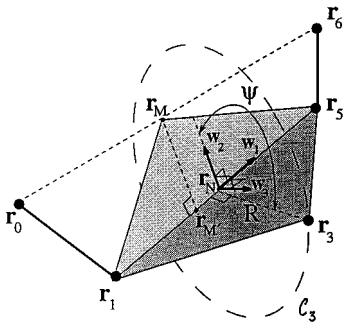

Figure 5. Frame of reference for describing the central trimer atom position. The position $\mathbf{r}_3$ is expressed in the frame [$\mathbf{w}_1$, $\mathbf{w}_2$, $\mathbf{w}_3$] with origin $\mathbf{r}_N$, where $\mathbf{r}_N$ is the projection of $\mathbf{r}_3$ onto the ($\mathbf{r}_1$, $\mathbf{r}_5$) axis. Unit vector $\mathbf{w}_2$ is parallel to ($\mathbf{r}_M$, $\mathbf{r}_{M'}$), where $\mathbf{r}_M$ is the midpoint of ($\mathbf{r}_0$, $\mathbf{r}_6$) and $\mathbf{r}_{M'}$ is the projection of $\mathbf{r}_M$ onto the ($\mathbf{r}_1$, $\mathbf{r}_5$) axis. The position of $\mathbf{r}_3$ on its locus is defined by the dihedral angle ψ between planes {$\mathbf{r}_1$, $\mathbf{r}_M$, $\mathbf{r}_5$} and {$\mathbf{r}_1$, $\mathbf{r}_3$, $\mathbf{r}_5$}. The locus of $\mathbf{r}_3$ is shown as the long-dashed circle C_3, centered at $\mathbf{r}_N$, of radius R, lying in a plane perpendicular to ($\mathbf{r}_1$, $\mathbf{r}_5$).

$$F_1[\mathbf{r}_2(\phi_L),\mathbf{r}_3(\psi)] = 0 \tag{1}$$

$$F_2[\mathbf{r}_4(\phi_R),\mathbf{r}_3(\psi)] = 0 \tag{2}$$

$$F_3[\mathbf{r}_2(\phi_L),\mathbf{r}_4(\phi_R)] = 0 \tag{3}$$

as shown in Appendix A.

The bridging equations (1)−(3) are highly nonlinear; it does not appear possible to solve them analytically for ϕ_L, ϕ_R, and ψ. It is possible, however, through substitution, to recast this set of equations to obtain a single equation in the variable ψ. Solving eqs 1 and 2 for ϕ_L and ϕ_R, respectively, yields two quadratic equations from which $\phi_L[\mathbf{r}_3(\psi)]$ and $\phi_R[\mathbf{r}_3(\psi)]$ can be determined analytically. Substituting these expressions into eq 3 results in the final equation, of the form

$$F(\psi) \equiv F_3[\mathbf{r}_2(\phi_L[\mathbf{r}_3(\psi)]),\mathbf{r}_4(\phi_R[\mathbf{r}_3(\psi)])] = 0 \tag{4}$$

as given in Appendix A. ψ provides a solution to the trimer bridging problem when $F(\psi) = 0$. The function $F(\psi)$ generally has four branches, because eqs 1 and 2 each contribute two roots for $\phi_L[\mathbf{r}_3(\psi)]$ and $\phi_R[\mathbf{r}_3(\psi)]$, respectively.

The numerical procedure for determining all values of ψ which satisfy eq 4 is discussed in the next subsection. After these values are obtained, $\phi_L[\mathbf{r}_3(\psi)]$ and $\phi_R[\mathbf{r}_3(\psi)]$ are calculated and $\mathbf{r}_2$, $\mathbf{r}_3$, and $\mathbf{r}_4$ are obtained directly from the expressions given in Appendix A.

3.3. Numerical Solution. With the trimer bridging problem cast entirely in terms of ψ, a numerical technique is presented to identify the roots ψ of the function $F(\psi)$ given in eq 4. As was explained in the previous section, the function $F(\psi)$ has, in general, four branches. The following discussion applies to the general case of finding *all* solutions on *all* branches.

As in the original CONROT scheme,[29] ψ values which satisfy eq 4 may exist over continuous but arbitrarily narrow, disjoint domains; this is exemplified by Figure 6b. There may be many roots for $F(\psi) = 0$. These roots may reside close to each other in ψ space (see Figure 6b near $\psi = -58°$); they may lie on different branches, and the values of torsion angles obtained from them may be quite different, as was demonstrated for CONROT.[29]

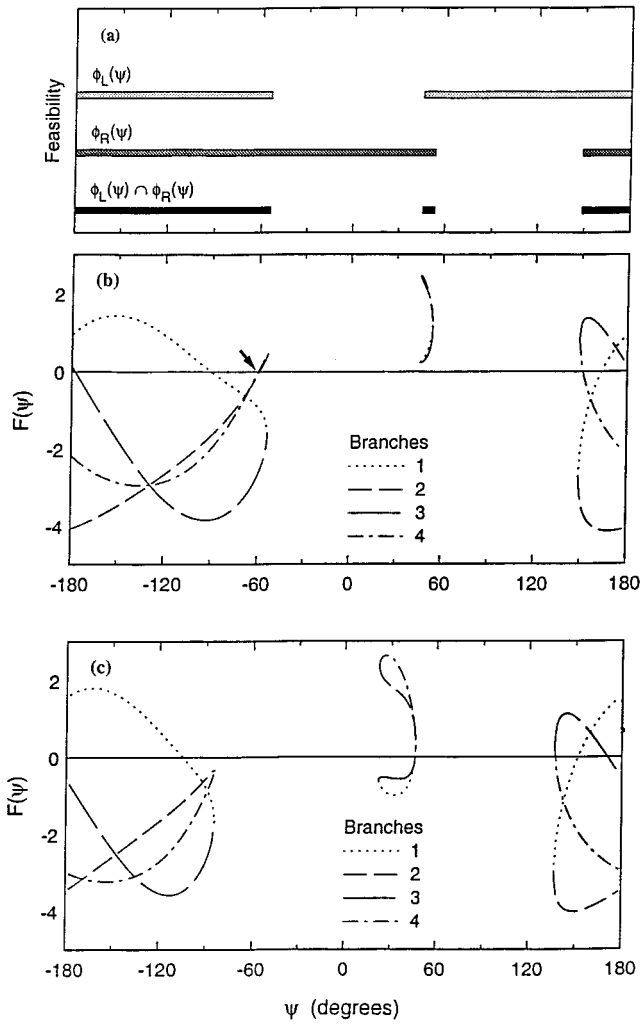

Figure 6. Typical shape and feasibility ranges of the trimer bridging function $F(\psi)$: Top: Feasibility regions for the existence of $F(\psi)$ in a typical local configuration of a model test chain about to undergo intramolecular rebridging (CONROT). Domains in ψ are shown for which real values of the following functions exist: $\phi_L(\psi)$ (light bars); $\phi_R(\psi)$ (medium-shaded bars); both $\phi_L(\psi)$ and $\phi_R(\psi)$ (dark bars). Middle: Plots of the four branches of the bridging solution function $F(\psi)$ for the initial configuration state for which feasibility regions are shown at the top. The different branches are displayed with different line types. $F(\psi)$ exists only where both $\phi_L(\psi)$ and $\phi_R(\psi)$ exist as real functions. In this case, $F(\psi)$ is defined in two disjoint ψ domains and yields six roots lying in one of the two domains. The arrow indicates the particular root ($\psi \approx -58°$) corresponding to the initial local chain configuration. Bottom: Plots of the four branches of the trimer bridging solution function $F(\psi)$ for a trial configuration state. The trial state was generated by performing a CONROT move on the state indicated by the arrow in the middle plot. Torsion angles $\phi_0 \equiv \phi_L$ and $\phi_7 \equiv \phi_R$ were driven by $-6.48°$ and $4.44°$, respectively. Two roots disappear near the initial configuration ($\psi \approx -58°$), and two new roots are created ($\psi \approx 45°$); in this case, the total number of roots (6) is conserved.

For some configurations of the dimers ($\mathbf{r}_0$, $\mathbf{r}_1$) and ($\mathbf{r}_5$, $\mathbf{r}_6$), there may be no solutions; it is possible that no branch of the function crosses the $F(\psi) = 0$ axis. It is also possible that $F(\psi)$ does not exist for *any* ψ value. For example, the $|\mathbf{r}_1 - \mathbf{r}_5|$ gap may be too large to be bridged under any orientation of a trimer with specified internal geometry.

To identify trimer bridging solutions, a "brute-force" sweep through the entire ψ space $(-\pi, \pi)$ could be performed, analogous to the sweep through ϕ_1 space employed in CONROT.[29] However, in the present formulation it is possible to determine, *in advance*, all ψ domains for which the bridging is feasible, i.e., for which the function $F(\psi)$ exists. Knowledge of the feasible domains prior to the numerical sweep through ψ space improves the robustness and computational efficiency of the numerical search scheme.

The conditions under which the trimer bridging problem is feasible are given in Appendix B. The simplest among them is based on the fact that $\mathbf{r}_3$ lies on the intersection of two spheres, one centered at $\mathbf{r}_1$ with radius $|\mathbf{r}_3 - \mathbf{r}_1|$ and one centered at $\mathbf{r}_5$ with radius $|\mathbf{r}_3 - \mathbf{r}_5|$. For the existence of such an intersection,

$$|\mathbf{r}_5 - \mathbf{r}_1| \leq |\mathbf{r}_3 - \mathbf{r}_1| + |\mathbf{r}_3 - \mathbf{r}_5| \tag{5}$$

If the dimers ($\mathbf{r}_0$, $\mathbf{r}_1$) and ($\mathbf{r}_5$, $\mathbf{r}_6$) form a bridging gap which violates eq 5, $F(\psi)$ does not exist for any ψ.

Additional feasibility conditions of the trimer bridging problem are derived from the discriminants of the quadratic equations from which $\phi_L[\mathbf{r}_3(\psi)]$ and $\phi_R[\mathbf{r}_3(\psi)]$ are determined; the discriminants must be non-negative for real geometric solutions to exist. This requirement is formulated as two quartic inequalities in $\tan(\psi/2)$. Each has four, two, or zero real roots, which can be determined analytically. For a given inequality, the roots and the sign of the fourth-order coefficient determine the ψ domains over which real values of ϕ_L or ϕ_R exist, as summarized in Appendix B. The intersection of these two sets of ψ domains defines a subset of domains over which *both* ϕ_L and ϕ_R exist (see Figure 6a); only ψ values *within* these domains can be solutions to the trimer bridging problem. On the basis of the knowledge of the feasible ψ domains, an exhaustive search for solutions is undertaken within each branch of $F(\psi)$.

The determination of all solutions for a given branch proceeds as follows. Initially, a scaled, pretabulated mesh of ψ nodes is mapped onto each one of the feasible domains. The use of this scaled mesh ensures the detection of solutions located in arbitrarily narrow domains (see Figure 6b). A vectorized sweep through the nodes is performed to calculate $F(\psi)$ at points throughout the domain. A second sweep is performed with the mesh displaced by a differential amount, allowing for a finite difference estimation of the gradient in $F(\psi)$. The value of $F(\psi)$ and the sign of the gradient at each mesh position are used to identify intervals within the domain that may contain a root. Each of these intervals is searched exhaustively using a weighted bisection method. The bisection proceeds until a tolerance limit is reached (indicating that no root exists within that interval) or until a smaller interval is located that is bracketed by points at which $F(\psi)$ assumes values of opposite sign. In the latter case, a Regula−Falsi algorithm[39] is employed to converge on the ψ value of the root with a tolerance of $\leq 10^{-8}$. Special strategies are employed to deal with the possibility of several roots existing within the same mesh interval; this can occur when maxima or minima of a given branch just glance the $F(\psi) = 0$ axis. The same numerical procedure is repeated for all domains and all branches, storing the resulting solution sets.

As with the original CONROT move, the extent of possible geometric solution searches in the intramolecular bridging construction can be limited to a predefined "wedge" of ψ space. This happens because of the existence of the initial local chain configuration which

corresponds to one out of a set of possible ψ solutions consistent with the initial configuration of the bridged dimers (e.g., the solution denoted by the arrow in Figure 6b). In a trial CONROT calculation, following rotation of the dimers by the driver angles, the ψ wedge of width $2W$, where $0 \leq W \leq \pi$, can be centered on the initial root position. The search for solutions can therefore *additionally* be confined to the intersection between the feasible ψ domains and the wedge $\psi_{\text{initial}} - W \leq \psi_{\text{trial}} \leq \psi_{\text{initial}} + W$. Reducing W below π was seen to limit the magnitude of configurational changes induced by each CONROT move but also to cut down on the computational effort required. In all simulations reported in this work, the full interval ($W = \pi$) of possible ψ values was included in the geometric search problem.

Trimer bridging functions $F(\psi)$ at the initial and trial states of a MC move may be significantly different. In the CONROT example shown in Figure 6b,c, the displacement of the flanking atoms ($\mathbf{r}_1$ and $\mathbf{r}_5$) brought about by the move altered the dimer positions enough to shift, annihilate, and create roots of $F(\psi) = 0$; two roots were annihilated near the initial configuration ($\psi \approx -58°$) and two new roots were created ($\psi \approx 45°$), conserving the original number of roots.

For $W = \pi$, the number of roots of the trimer bridging function $F(\psi)$ varies greatly with configuration but is always even, with an average of approximately 6.[29] In general, the number of roots depends on the magnitude of the search wedge W employed.

3.4. Algorithm Implementation. To facilitate the implementation of the EB move, special lists are maintained with candidates for bridging around each chain end. The criterion for inclusion in these "end-bridging" lists is that the candidate atom must be an internal segment of another chain within the all-trans bridging distance ($=4l\cos(\theta_0/2)$) of a particular chain end, where l is the carbon−carbon bond length and θ_0 is the supplement of the C−C−C equilibrium bond angle. The number of bridgeable neighbors $N_{\text{bridge}}(p)$ of each chain end p in the system is continuously updated and enters into the acceptance criterion of the MC move.

Under the assumption of a classical flexible model in the limit of infinite bond stretching force constants,[40] EB and CONROT moves from an initial state m to a final state n are accepted with probability which is given by eq 6 in ref 30. J in this equation is the Jacobian determinant accounting for the local coordinate transformation from Cartesian to *constraint* variables implicit in employing the trimer bridging construction as a Monte Carlo move. This transformation is nonmetric preserving and calls into effect Jacobians relating differential volume elements in the two coordinate systems: To within a constant, J is equal to the ratio of a volume element in Cartesian coordinate space over the corresponding volume element in the constraint variable space. The need for such Jacobians was first encountered in the initial CONROT work,[29] where a methodology for their calculation was also given. Pant and Theodorou[30] generalized the formulation of J to take into account that, in double-driven CONROT and EB moves, all coordinates of the heptamer centered at the bridge need to be considered. (In the initially formulated unidirectional CONROT move,[29] only one of the dimers neighboring the trimer bridge is changed, and this simplifies the calculation of J somewhat.) Although the expression given by Pant and Theodorou[30] is perfectly correct, a new, more transparent and computationally more efficient expression for J was developed and used in the present study. Its derivation is given in Appendix C, along with a complete discussion of alternative coordinate systems that can be used for the description of the trimer and of transformations between these systems.

4. Simulation Method

4.1. Strategy. In the present study, a number of linear PE melts of various number-average degrees of polymerization $\bar{X}$ (measured in CH_2- and CH_3-mers) were simulated. The chain-length distribution was in all cases uniform in the closed interval from $\bar{X}(1 - \Delta)$ to $\bar{X}(1 + \Delta)$, where Δ denotes the half-width of the chain-length distribution reduced by the number-average chain length. The following systems were simulated at a value of $\Delta = 0.5$: a 40-chain C_{78} melt ($\bar{X} = 78$, polydispersity index $I = 1.085$); a 20-chain C_{156} melt ($\bar{X} = 156$, $I = 1.084$); a 16-chain C_{200} melt ($\bar{X} = 200$, $I = 1.084$); a 10-chain C_{400} melt ($\bar{X} = 400$, $I = 1.084$); an 8-chain C_{500} melt ($\bar{X} = 500$, $I = 1.083$). Clearly, melts of the same Δ have chain-length distributions of the same shape. The value of Δ is related to the polydispersity index I, defined here as the ratio of the second moment to the squared first moment of the chain-length distribution, by the following equation, which becomes exact in the limit of long chains, where the distribution of chain lengths can be considered as continuous:

$$I = 1 + \Delta^2/3 \tag{6}$$

To investigate the effect of the chain-length distribution function on the performance of the end-bridging algorithm, especially when that distribution function gets narrow, additional simulations were executed on each of the longer-chain systems C_{200}, C_{400}, and C_{500} with Δ values ranging from 0.6 to 0.3. The results from all of these simulations will be discussed in detail in the subsequent sections. In these sections, occasional reference will be made also to results obtained from the simulations on two smaller C_{24} and C_{78} chain systems, containing 10 chains of C_{78} and 32 chains of C_{24}, respectively, as well as from an additional simulation on a larger C_{200} system containing 25 chains of C_{200}. These results will help quantify more precisely the limits of transition from a short-alkane to a truly polymeric behavior as the chain length is increased. They will also allow us to compare the performance of the EB code with other MC and MD methods and to assess different molecular models in terms of their ability to predict structural and volumetric properties.

All simulations have been conducted at pressure $P = 1$ atm and temperature $T = 450$ K and consisted of two steps: The first step involved the generation of an initial configuration, from which the end-bridging MC simulation was started. All initial configurations were generated by employing the three-stage constant-density energy minimization technique of Theodorou and Suter,[16] to generate structures trapped at a local energy minimum with density equal to the experimental value under the P and T conditions of the simulation.

Thermal equilibration of the melt followed, using EB Monte Carlo. The simulations were conducted in the semi-grand canonical ensemble of Pant and Theodorou,[30] with a relative chemical potential profile designed to give the uniform chain-length distributions stated

above. The following mix of moves was used in all simulations: 6% reptations, 6% rotations, 6% flips, 32% CONROT, 49.5% end bridging, and 0.5% volume fluctuations. The flip[33] is a very simple move involving the random selection of an internal chain segment and its rotation about the axis joining its two neighboring segments on the same chain by a small random angle. This move leaves the bond lengths unchanged but modifies up to two bond angles and up to four dihedral angles. Volume fluctuations are initiated by randomly expanding or contracting all edge lengths of the periodic box by a random amount. The starts of all chains are affinely displaced following the isotropic deformation of the periodic box, with all bond lengths, bond angles, and torsion angles left unchanged.

In the case of reptations, rotations, and flips, the attempt probabilities α are equal for the forward ($m \rightarrow n$) and reverse ($n \rightarrow m$) moves. Because these moves involve only *independent* degrees of freedom, no Jacobians are required. Therefore, the acceptance probability for these moves reduces to the usual canonical-ensemble Metropolis selection criterion. In the acceptance criteria for a volume fluctuation, attempt probabilities and Jacobians again cancel, but volume terms must be accounted for in the equation for the acceptance probability.[30]

4.2. Important Aspects of the Code. Key to the efficiency of the code has been the use of lists, each containing structured information about the current configuration of the system, which find immediate application in attempting MC moves. Use is made primarily of the following four lists:

(1) *A screening overlap list*, created by dividing the system into a large number of small cells of dimension a little larger than the LJ diameter σ. This list is useful in rapidly discarding attempted moves which would result in large excluded-volume overlaps.

(2) *A linked-cell list*, created by dividing the system into a certain number of cells, each of linear dimension at least equal to the sum of the LJ cutoff distance plus a "skin". A relatively small number ($4 \times 4 \times 4$ or $5 \times 5 \times 5$) of linked cells of edge length around 10 Å was used in our simulations, but, in general, this number is determined by the size of the system. With this list, the search for intra- and intermolecular neighbors is restricted to only within the cell where the reference segment resides and its 26 nearest-neighbor cells.

(3) A usual *Verlet neighbor list*[6] containing the intra- and intermolecular neighbors found within the 27 nearest linked cells. A fixed skin thickness of about 1 Å was used for this list.

(4) An *end segment neighbor list*, which, for each end segment, gives all segments on other chains with which end bridging is feasible. Like the Verlet list, the end list also employs a "skin", whose thickness was fixed at 0.3 Å in all of our simulations.

All four lists are initially created at the beginning of the simulation and updated in the course of the MC run. The most significant outcome of making extensive use of the lists in the simulations is that the CPU time spent per Monte Carlo iteration (i.e., per attempted MC move) remains almost constant, exhibiting only a very weak dependence on chain molecular characteristics and the size of the simulation box. This can be seen in Table 2, which presents CPU time data collected from runs on all systems investigated in the present work (C_{78}, C_{156}, C_{200}, C_{400}, and C_{500}, all in a box with an average edge length of around 45−50 Å, as well as a smaller system, the 10-chain C_{78}, in a box with an average edge length of around 29 Å, referred to as the "smaller C_{78}" system). Times needed for the systems to execute 1 million MC iterations on an SGI 64-bit R10000 processor, with the mix of moves reported in the previous subsection, are reported in the table.

Table 2. CPU Time Required for the System To Execute 1 Million MC Attempted Moves[a]

system	total sites, n	effective interacting sites	CPU time (s)
C_{78} (smaller)	780	780	2450 ± 50
C_{78}	3120	1316	4200 ± 100
C_{156}	3120	1316	4100 ± 100
C_{200}	3200	1350	4350 ± 100
C_{200} (larger)	5000	1080	3500 ± 100
C_{200} ($\Delta = 0.375$)	3200	1316	3800 ± 150
C_{200} ($\Delta = 0.25$)	3200	1316	3700 ± 150
C_{400}	4000	1688	5400 ± 100
C_{400} ($\Delta = 0.4$)	4000	1688	5200 ± 150
C_{400} ($\Delta = 0.3$)	4000	1688	5200 ± 150
C_{500} ($\Delta = 0.6$)	4000	1688	5500 ± 100
C_{500} ($\Delta = 0.55$)	4000	1688	5400 ± 100
C_{500}	4000	1688	5400 ± 100
C_{500} ($\Delta = 0.4$)	4000	1688	5300 ± 100
C_{500} ($\Delta = 0.3$)	4000	1688	5200 ± 150

[a] The mix of moves is described in the text. Runs are on an SGI 64-bit R10000 processor at 195 MHz ($T = 450$ K and $P = 1$ atm). Δ is equal to 0.5, unless otherwise indicated.

Three points are notable in Table 2: First, systems that are of equal size, i.e., contain the same number of interacting sites, require the same CPU time per MC iteration. On the average, this time is 2.4×10^{-3} CPU s/MC iteration for the two smaller systems containing about 780 interacting sites, 4.2×10^{-3} CPU s/MC iteration for the systems containing about 3200 interacting sites, 5.3×10^{-3} CPU s/MC iteration for the systems containing 4000 interacting sites, and 3.5×10^{-3} CPU s/MC iteration for the larger C_{200} system containing 5000 interacting sites. From these figures it is not immediately obvious that the CPU time/MC iteration remains constant in all of our simulations. To see this, one must take into account that the rate-controlling step of the simulation is the evaluation of interactions, and this scales with the number of potentially interacting sites considered for each site displaced in a move. This number depends on how we split our simulation box into subboxes (cells) in our linked-cell list scheme. The systems containing about 3200 interacting sites are split into $4 \times 4 \times 4$ linked cells, each cell containing on the average $3200/64 \approx 50$ interacting sites. Therefore, the 27 neighboring cells that need to be considered in every attempted MC move contain on the average a total of $27 \times 50 \approx 1350$ interacting sites. We term these *effective interacting sites*. For the systems containing 4000 interacting sites, the corresponding number of effective interacting sites is about 1700. On the other hand, for the larger C_{200} system, containing 5000 interacting sites, the simulation box is split into $5 \times 5 \times 5 = 125$ linked cells, and therefore the number of effective interacting sites is only about 1100. The reader can then immediately see that the CPU times are, to an excellent approximation, proportional to the number of effective interacting sites that need to be considered in each system. Independently of the total size of the system, therefore, the CPU time τ spent per MC iteration in our simulations can be considered to be a constant, to an excellent approximation. In the present

Table 3. Percent Acceptance Rates of the MC Moves Used in the Simulations as a Function of System Size, Average Chain Length $\bar{X}$, and Chain-Length Distribution Δ[a]

system	reptation	rotation	flip	CONROT	end bridge	volume fluctuation
C_{78}	6.9 ± 0.1	16.2 ± 0.2	76.8 ± 0.1	19.5 ± 0.3	0.090 ± 0.001	30.1 ± 0.5
C_{156}	6.9 ± 0.2	16.1 ± 0.2	76.8 ± 0.2	19.5 ± 0.3	0.090 ± 0.001	20.8 ± 0.5
C_{200}	6.7 ± 0.2	16.1 ± 0.2	76.8 ± 0.2	19.3 ± 0.3	0.089 ± 0.001	19.0 ± 0.5
C_{200} (larger)	6.7 ± 0.2	16.0 ± 0.2	76.8 ± 0.2	19.3 ± 0.3	0.089 ± 0.001	19.0 ± 0.5
C_{200} ($\Delta = 0.375$)	6.6 ± 0.2	16.0 ± 0.2	76.7 ± 0.2	19.4 ± 0.3	0.077 ± 0.001	18.7 ± 0.5
C_{200} ($\Delta = 0.25$)	6.5 ± 0.2	15.7 ± 0.2	76.8 ± 0.2	19.4 ± 0.3	0.063 ± 0.001	18.2 ± 0.5
C_{400}	6.6 ± 0.2	16.1 ± 0.2	76.8 ± 0.2	19.4 ± 0.2	0.089 ± 0.001	12.2 ± 0.3
C_{400} ($\Delta = 0.4$)	6.6 ± 0.2	16.0 ± 0.2	76.8 ± 0.2	19.4 ± 0.2	0.080 ± 0.001	12.2 ± 0.3
C_{400} ($\Delta = 0.3$)	6.4 ± 0.2	15.7 ± 0.2	76.8 ± 0.2	19.4 ± 0.2	0.069 ± 0.001	12.0 ± 0.3
C_{500} ($\Delta = 0.6$)	6.6 ± 0.2	16.0 ± 0.2	76.7 ± 0.2	19.4 ± 0.2	0.096 ± 0.002	11.2 ± 0.3
C_{500} ($\Delta = 0.55$)	6.6 ± 0.2	16.0 ± 0.2	76.7 ± 0.2	19.4 ± 0.2	0.092 ± 0.002	11.2 ± 0.3
C_{500}	6.6 ± 0.2	16.0 ± 0.2	76.7 ± 0.2	19.4 ± 0.2	0.089 ± 0.001	11.3 ± 0.3
C_{500} ($\Delta = 0.4$)	6.7 ± 0.2	16.0 ± 0.2	76.7 ± 0.2	19.4 ± 0.2	0.080 ± 0.001	11.2 ± 0.3
C_{500} ($\Delta = 0.3$)	6.2 ± 0.2	15.5 ± 0.3	76.7 ± 0.2	19.4 ± 0.2	0.069 ± 0.001	11.2 ± 0.3

[a] Wherever the value of Δ is not explicitly indicated, $\Delta = 0.5$. System sizes are reported in Table 2. $T = 450$ K and $P = 1$ atm.

work we will use the symbol τ to denote the CPU time per iteration in a system with 4000 sites and 1688 effective interacting sites. This quantity is

$$\tau = 5.3 \times 10^{-3} \text{ CPU s/MC iteration} \qquad (7)$$

CPU times from systems with different effective numbers of interaction sites will be rescaled to reflect this constant value of τ.

A second observation on the data of Table 2 is that, upon decreasing Δ (the reduced width of the MW distribution function), the CPU time per MC iteration drops somewhat. This is only a minor decrease and is due to the fact that, when Δ decreases, the acceptance rate of the end-bridging move also decreases somewhat (see discussion in the next paragraphs). This causes a smaller number of list updates, which eventually results in some savings in the CPU time.

A third point to notice about Table 2 is the small magnitude of all CPU times reported: on average, all systems studied in this work need less than about 5000 s to execute 10^6 MC iterations. As we shall see in the next section, a total of about 50×10^6 MC iterations is enough for the system to equilibrate not only its volumetric but also its long-range conformational properties. This means that, with the EB method, about a week on a powerful workstation is sufficient for fully equilibrating a long-chain polymer system, such as the 8-chain C_{500} PE melt studied in the present work.

Table 3 presents results for the acceptance rates of all six MC moves employed in our simulations as functions of the size of the system, the average chain length $\bar{X}$, and the reduced width of the chain length distribution function Δ. The very low acceptance rates of the EB move are evident for all systems: only about 0.1% of the attempted moves are accepted. Despite this, however, the results of the next section will show that the EB move is orders of magnitude more effective than any other atomistic simulation scheme we are aware of in vigorously sampling the long-range conformational properties of long polymers. For the same values of $\bar{X}$ and Δ, the size of the system (total number of interacting sites n) has no effect on the acceptance rate of EB. Similarly, as seen in Table 3, for high enough chain lengths, the acceptance rate of EB is insensitive to mean chain length $\bar{X}$. What does affect the EB acceptance rate the most is Δ: for the same system size and average chain length $\bar{X}$, the acceptance rate drops significantly with decreasing Δ; i.e., the narrower the chain-length distribution gets, the less effective the end-bridging move becomes. This decrease is quantified in Appendix D, where it is shown that, to an excellent approximation, the EB acceptance rates p_{acc} reported in Table 3 drop with decreasing Δ as $\Delta^{0.5}$.

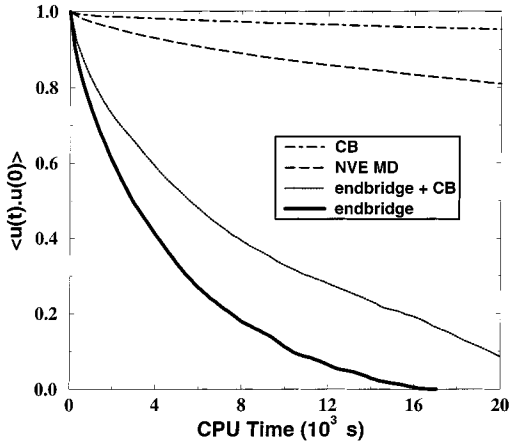

Figure 7. Decay of the chain end-to-end vector orientational autocorrelation function $\langle \mathbf{u}(t) \cdot \mathbf{u}(0) \rangle$ for the "smaller" C_{78} chain system obtained with (a) the NPT configurational bias MC method (dot-dashed line), (b) the NVE MD method (dashed line), and (c) the present end-bridging MC method (solid line). Also shown is the curve obtained with the end-bridging MC method where 50% of the attempted end-bridging moves have been replaced by configurational bias moves (dotted line) ($T = 450$ K and $P = 1$ atm).

5. Results and Discussion

5.1. Computational Efficiency. The ability of the EB Monte Carlo method to fully equilibrate a long polymer system is first demonstrated in Figure 7, which displays results for the evolution of the orientational autocorrelation function $\langle \mathbf{u}(t) \cdot \mathbf{u}(0) \rangle$ of a unit vector directed along the chain end-to-end vector with CPU time, as obtained from runs in the smaller C_{78} PE melt system by four different simulation methods. The rate with which $\langle \mathbf{u}(t) \cdot \mathbf{u}(0) \rangle$ drops to zero is a measure of how fast the system forgets its initial configuration and, therefore, provides a measure to the effectiveness of the simulation method in equilibrating the system.

Starting from the bottom of Figure 7, the lowermost (solid) curve represents the results obtained by the present ($NnPT\mu^*$) EB Monte Carlo method, with the mix of moves mentioned in section 4.1; this is clearly the most effective of all. In the second curve (dotted), half of the end-bridging moves have been replaced by configurational bias (CB) ones (keeping the type and

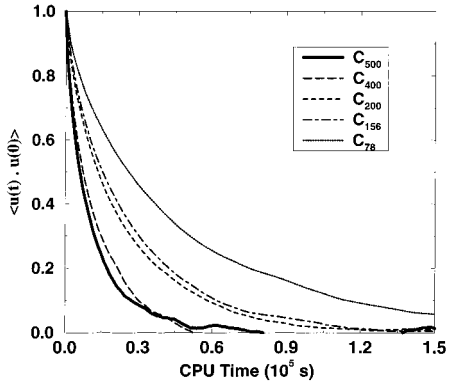

Figure 8. Decay of the chain end-to-end vector orientational autocorrelation function $\langle \mathbf{u}(t)\cdot\mathbf{u}(0)\rangle$ with CPU time, as obtained with the present EB algorithm, for various PE melt systems with mean chain length $\bar{X}$ ranging from C_{78} to C_{500} and $\Delta = 0.5$. CPU times have been corrected so that they correspond to the same number n (=4000) of mers in the periodic box for all systems ($T = 450$ K and $P = 1$ atm).

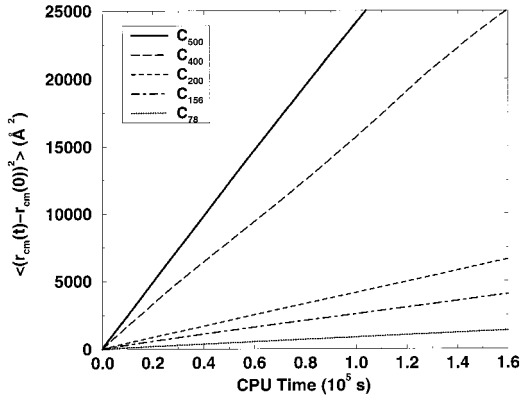

Figure 9. Mean-square displacement of the chain center of mass $\langle(\mathbf{r}_{cm}(t) - \mathbf{r}_{cm}(0))^2\rangle$ as a function of CPU time, obtained with the present EB algorithm, for all five PE mean chain lengths studied in the present work. $\Delta = 0.5$ in all cases. CPU times have been corrected so that they correspond to the same number n (=4000) of mers in the periodic box for all systems ($T = 450$ K and $P = 1$ atm).

attempt probabilities of all other moves in the mix unaltered), which seems to considerably degrade the performance of the method. If, in fact, all end-bridging moves are replaced by CB ones (keeping always the mix of the rest of the moves unaltered), the curve obtained is the uppermost (dot-dashed) curve. CB, without any end-bridging moves, is clearly unable to equilibrate long-range conformational properties for this chain length after 20×10^3 CPU s. Also shown in the figure is the curve obtained from an NVE MD run using the same potentials and incorporating a Fixman potential to ensure that the probability density sampled is identical to that of the MC.[34] MD is more effective than the CB Monte Carlo method; however, the figure shows it to be almost 2 orders of magnitude less effective than EB.

Figure 7 clearly shows that neither CB nor MD can relax the small C_{78} system within the limits of the available CPU time. Both methods fail to sample configurations that differ substantially in long-range conformational properties of the relatively long C_{78} chains, and for most of the simulation time the system remains trapped in the vicinity of its initial configuration. It is only with the powerful EB move that such drastic changes are induced in the system connectivity as to cause $\langle \mathbf{u}(t)\cdot\mathbf{u}(0)\rangle$ to drop to zero within the available simulation time. This demonstrates the superiority of EB over all currently known simulation methods for the equilibration of atomistic model polymer systems.

An important observation about the efficiency of EB is that it is significantly impacted by leaving out reptations: Indeed, if reptations are completely excluded from the cocktail of moves used in the simulation, the performance of the EB move drops dramatically. This happens because of two reasons: (a) only a few of the EB moves get accepted and (b) many of the EB moves are performed in the reverse direction to previous moves; thus, successive moves tend to annihilate each other. When reptations are included among the attempted moves, the end segment neighbor list is continuously refreshed, and this leads to an increase in the efficiency of the EB moves.

Figure 8 concerns the performance of EB when applied to the five longer-chain systems, C_{156}, C_{200}, C_{400}, and C_{500}, all with $\Delta = 0.5$ (compare Table 2). As already stated above, all CPU times reported in this figure have been normalized for possible differences in the number of effective interaction sites; further, they have also been normalized for the different system sizes (different n values). The figure shows quite convincingly that EB can fully equilibrate all of these systems within modest CPU time. What is more surprising about the results in this figure is that the longer the mean chain length $\bar{X}$, the faster the system is equilibrated with the EB method! As $\bar{X}$ increases, the $\langle \mathbf{u}(t)\cdot\mathbf{u}(0)\rangle$ curve decays faster. This is a unique feature of the EB method. It sets it apart from all other simulation techniques currently available, whose performance is always a strongly decreasing function of chain length.

To better quantify the performance of EB as a function of chain length, we also accumulated the mean-square displacement of the chain center of mass as a function of CPU time at constant system size and polydispersity ($\Delta = 0.5$) for the five chain lengths studied in the present work; this is shown in Figure 9. Results for C_{500}, C_{400}, C_{200}, C_{156}, and C_{78} are shown as solid, dashed, short-dashed, dot-dashed, and dotted lines, respectively. As in Figure 8, the CPU times reported here have been normalized for differences in the number of effective interaction sites and in the total number of interaction sites (n values). The figure shows quite clearly that the EB method "forces" the longer chains to diffuse faster than the shorter ones. Mathematically, the computational requirements for equilibrating each melt system can be quantified by calculating the CPU time t_0 needed for the mean-square displacement of the chain centers of mass in each system to become equal to the equilibrium mean-square end-to-end distance of the polymer, $\langle R^2\rangle$. For the C_{78} system, $t_0 = 1.7 \times 10^5$ s; for C_{156}, $t_0 = 1.2 \times 10^5$ s; for C_{200}, $t_0 = 1.0 \times 10^5$ s; for C_{400}, $t_0 = 0.5 \times 10^5$ s; and for C_{500}, $t_0 = 0.43 \times 10^5$ s.

The unique capability of the EB Monte Carlo method to equilibrate the longer-chain melts faster can, in fact, be predicted by analytical arguments, if one considers the configurational changes induced by an end-bridging move. Such an analysis permits calculation of the mean-square displacement of the centers of mass of the two chains involved in the end-bridging move, averaged over all configurations in the system. A detailed derivation is presented in Appendix D. The analysis is based on the premise that all chains and subchains participating

in the EB move behave as random coils, a condition best satisfied for the longer-chain systems studied here. The analysis makes use of the fact that the CPU time τ spent per Monte Carlo iteration with our algorithm is practically independent of the size of the system (see above). The CPU time t_0 provides a direct measure of the efficiency with which the method tracks the longest relaxation time of the melt system. Results for t_0 are presented in terms of four variables: the first is the CPU time τ per Monte Carlo iteration given by eq 7; the second is the system size (number of segments n); the third is the average chain length $\bar{X}$; and the fourth is the reduced width Δ of the chain length distribution function, related to the polydispersity index I through eq 6. The final equation is

$$t_0 \approx K\tau \frac{n}{\bar{X}\Delta^{2.5}} \tag{8}$$

with K a constant independent of the system size and MW distribution. According to eq 8, for the given system size and shape of the chain-length distribution function (i.e., keeping n and Δ constant), the equilibration time for the end-bridging algorithm should scale inversely with the mean chain length ($t_0 \propto \bar{X}^{-1}$). This is in sharp contrast to actual Rouse dynamics, where $t_0 \propto \bar{X}^2$, or to reptation dynamics, where $t_0 \propto \bar{X}^3$. Equation 8 further shows that t_0 should scale as n^1: this is a mere consequence of the fact that the CPU time τ per Monte Carlo iteration is constant, provided the number of effective interacting sites considered in each move is constant (see above). Thus, if n is doubled, keeping all intensive properties of the system constant, the simulation time must be doubled for every degree of freedom to experience the number of moves required for equilibration to occur. Equation 8 also shows that t_0 should increase with decreasing Δ as $(1/\Delta)^{2.5}$. This strong dependence might suggest at first sight that the method requires broad distributions of molecular lengths (i.e., large polydispersity) in order to be effective. As we shall see shortly, however, melts with $\Delta = 0.35$ ($I = 1.04$) can be simulated with very reasonable computational resources; the method remains viable down to very low degrees of polydispersity, comparable to the ones achieved with anionic polymerization techniques. Furthermore, the conformational and thermodynamic properties of the melt are insensitive to the Δ value assumed, at least as long as Δ is kept less than about 0.5.

In Figure 10, the dependence of t_0 on $\bar{X}$ suggested by eq 8 is examined by plotting on a log−log plot t_0 versus $\bar{X}$ at constant n and Δ for the test runs we performed, with the CPU times having been obtained directly from the data of Figure 9. A continuously decreasing curve is obtained, which, for values of $\bar{X} \geq 156$, approaches a straight line. The slope of this line (dashed line in the figure) is ≈ -1.0, in excellent agreement with eq 8. The scaling law described by eq 8 and supported by the simulation findings of Figure 10 is the strongest evidence of the unique capability of the end-bridging algorithm to simulate efficiently dense, truly polymeric systems.

Figure 11 shows the mean-square displacement of chain centers of mass as a function of CPU time for the C_{500} PE melts with $n = 4000$, characterized by different Δ values. When Δ is decreased, the diffusive progress of the chains is seen to be slowed down considerably.

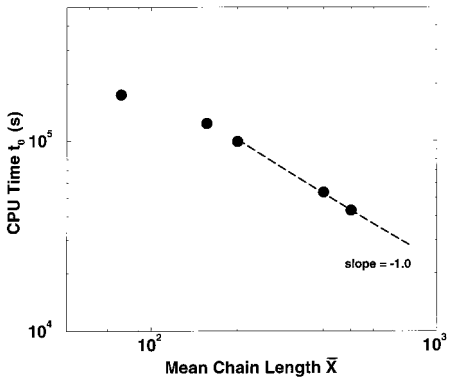

Figure 10. CPU time t_0 required for the mean-square displacement of the chain center of mass to reach the equilibrium mean-squared end-to-end distance $\langle R^2 \rangle$ versus average chain length $\bar{X}$ on a log−log plot. t_0 has been corrected, so that it corresponds to the same number n (=4000) of mers in the periodic box for all systems. For $\bar{X} \geq 156$, the simulation data approach a straight line (dashed line in the figure) with slope ≈ -1.0, in excellent agreement with the scaling law of eq 8 ($\Delta = 0.5$, $T = 450$ K, and $P = 1$ atm).

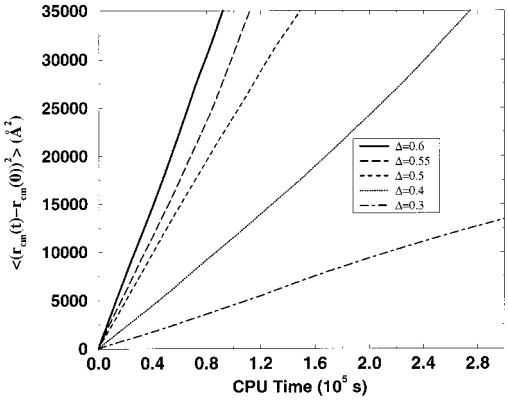

Figure 11. Mean-square displacement of the chain center of mass $\langle(\mathbf{r}_{cm}(t) - \mathbf{r}_{cm}(0))^2\rangle$ as a function of CPU time, obtained with the EB algorithm, for the longest C_{500} system and for various values of the parameter Δ characterizing the breadth of the chain-length distribution ($T = 450$ K and $P = 1$ atm).

By calculating t_0 from the figure, we can construct the log−log plot of t_0 versus Δ shown in Figure 12. In the region of $\Delta \geq 0.5$ the curve approaches a straight line of slope $\simeq -2.5$ (lower dashed line in the figure), exactly as suggested by eq 8. As Δ decreases below 0.5, however, the dependence of t_0 on Δ becomes stronger. The curve now approaches a straight line with a slope of $\simeq -3.5$ (upper dashed line in the figure).

Simulation data for $\Delta < 0.5$ at $\bar{X} = 500$ in Figure 12 depart from the scaling prediction of eq 8 because the subchains cut from the victim chain and annexed by the attacking chain in an end-bridging move are not long enough to behave as random coils, thus not fulfilling the premises on which the derivation of Appendix D rests. At low Δ, the subchains exchanged between victim and attacking chains are short, so that the two chains formed after the move do not violate the upper and lower bounds of the MW distribution function. With only short subchains exchanged, the efficiency of the end-bridging move drops rapidly, and this shows up as a sharp increase in the slope of Figure 12 for Δ values below 0.5. Clearly, for systems of higher mean chain length $\bar{X}$, the critical Δ value below which the $\Delta^{-2.5}$ scaling breaks down is expected to shift to smaller values.

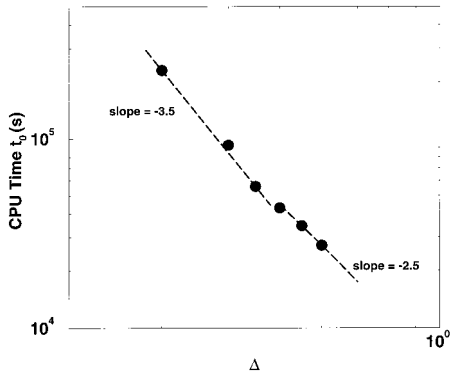

Figure 12. CPU time t_0 required for the mean-square displacement of the chain center of mass to reach the equilibrium mean-squared end-to-end distance $\langle R^2 \rangle$, versus the reduced width Δ of the chain-length distribution on a log−log plot (C_{500}, $T = 450$ K, and $P = 1$ atm). t_0 has been corrected so that it corresponds to the same number n (=4000) of mers in the periodic box for all systems. For $\Delta \geq 0.50$, the simulation data approach a straight line (lower dashed line in the figure) with slope ≈ -2.5, in excellent agreement with the scaling law of eq 8. For $\Delta \leq 0.50$, the best linear fit to the simulation data (upper dashed line in the figure) is a straight line with slope -3.5 ± 0.2.

Collected results for the characteristic time t_0 calculated for the various systems studied in the present work are reported in Table 4. By comparing the CPU times t_0 for the "smaller" and the "larger" C_{78} systems, in particular (n values given in Table 2) one confirms that an increase in system size by a factor of 4 (keeping $\bar{X}$ and Δ constant) results in an increase of t_0 by the same factor. In other words, the scaling $t_0 \propto n^1$ of eq 8 is confirmed by our simulation results. The same scaling is also seen to be true when one compares the results for the C_{200} and the "larger" C_{200} chain systems.

5.2. Conformational Properties. The ability of the end-bridging move to relax the long-range conformational characteristics of long-chain systems is demonstrated in Figures 13 and 14, presenting the relaxation of the mean-square end-to-end distance $\langle R^2 \rangle$ and of the mean-square radius of gyration $\langle R_g^2 \rangle$, for the longest (C_{500}) chain system studied in the present work. After an initial equilibration period, which depends on the size and MW distribution as discussed above, both $\langle R^2 \rangle$ and $\langle R_g^2 \rangle$ are seen to approach constant values. Upon decreasing Δ, i.e., upon decreasing the polydispersity of the system, the equilibration of both $\langle R^2 \rangle$ and $\langle R_g^2 \rangle$ slows down; however, the final, equilibrium values are practically the same, suggesting a negligible effect of Δ on the equilibrium conformational properties. For this chain length, equilibrium values of $\langle R^2 \rangle$ and $\langle R_g^2 \rangle$ obey the random-coil relation $\langle R^2 \rangle = 6\langle R_g^2 \rangle$ to an excellent approximation.

Results for $\langle R^2 \rangle$ and $\langle R_g^2 \rangle$ for relatively short-chain systems, for all three molecular models used in the simulations, are collected as functions of $\bar{X}$ in Tables 5 and 6. $\langle R^2 \rangle$ values for all chain lengths X encountered in our C_{24} and C_{78} simulations are plotted in Figure 15. Also shown in the tables and figures are the results obtained by sampling continuous unperturbed chains (CUCs) corresponding to each molecular model used. CUC chains are defined[30,31,33] as isolated chains governed by exactly the same potentials as the melt chains but devoid of nonlocal interactions along their contours. More specifically, the bond angle bending and torsional potentials of a CUC are identical to those acting on the bulk chains. The LJ potential is also identical but active only between mers separated by four skeletal bonds along the contour (pentane effect), consistent with the definition of local interactions used by Flory in his development of rotational isomeric state (RIS) models.[32] For given values of (N, n, P, T, $\boldsymbol{\mu}^*$), CUCs are easily sampled using configurational bias[26] and generalized reptation moves.[30,33]

Tables 5 and 6 and Figure 15 show that the conformational characteristics of chains in the well-equilibrated melt are practically indistinguishable from those of CUCs for all three molecular models. This has been established in several other works on PE[30,31,38,41] but is not a general conclusion for all polymers.[42] Because the conformational characteristics of bulk melt chains and CUCs are indistinguishable, we can perform MC simulations with CUCs on long-chain systems to calculate the characteristic ratio C_X as a function of the number of bonds X for all three models of interest. The results are shown in Figure 16, which presents the scaled chain mean-square end-to-end distance $\langle R^2 \rangle / [(X-1)l^2]$ as a function of the inverse number of bonds $1/(X-1)$ along the chain. For all three models, C_∞ can be calculated by extrapolating the corresponding curve to intersect the y axis. The following values are found for C_∞: 9.13 (this model); 8.30 (Yoon et al. model); 9.60 (Smit et al. model).

All of these values are significantly larger than the value 6.7 reported for real PE,[1,9] which means that the torsional potentials employed enhance trans conformational states. Of the three models, the Yoon et al. model seems to produce the most realistic conformations, especially in view of recent experimental measurements, which have yielded $C_\infty = 7.8$ in the melt state.[43,44]

For the molecular model used in the present work, detailed results for the dependence of $\langle R^2 \rangle$ on chain length obtained from CUC chains in the regime C_{12}−C_{117} allowed us to derive an analytical expression for the function $\langle R^2 \rangle = \langle R^2 \rangle(X)$ (eq 21 in ref 33). In Figure 17, we show how this analytical expression compares with new results from the present simulations on the longest (C_{500}) system studied ($\Delta = 0.5$). The thin solid line displays the simulation results, the thick dotted line represents the best linear fit to these results, and the thick long-dashed curve represents the predictions of the analytical expression. The solid line was obtained from one single simulation and presents $\langle R^2 \rangle$ for all chain lengths present in the system (from C_{250} to C_{750}); this explains the large noise in the data. The good agreement between the thick dotted and the thick long-dashed lines in Figure 17 demonstrates that eq 21 of ref 33 is applicable to much longer-chain systems than those used to derive it and confirms the good equilibration and internal consistency of our EB results. The small discrepancies seen in the long-chain regime are due to the noise of the simulation data rather than to an inadequacy of the CUC-based analytical equation to represent chain dimensions in the bulk. Evidence for this is provided by the fact that running the simulation for longer times is seen to reduce the gap between the linear fit to the $\langle R^2 \rangle(X)$ results and the prediction of the analytical equation.

5.3. Relaxation of the Chain Internal Structure. In section 5.1 we have presented evidence that the EB algorithm ensures extremely rapid equilibration of the overall chain dimensions. The question arises as to whether more local, internal structural features are equilibrated with comparable efficiency. To address this

Table 4. Observed Values of the Characteristic Time t_0, in 10^5 CPU s, Needed for the Chain Center of Mass Mean-Square Displacement To Reach the Mean-Square Chain End-to-End Distance for All Systems Simulated[a]

system	CPU time	system	CPU time	system	CPU time
C_{78} (smaller)	0.45 ± 0.05	C_{200} ($\Delta = 0.375$)	2.5 ± 0.1	C_{500} ($\Delta = 0.6$)	0.28 ± 0.05
C_{78}	1.7 ± 0.1	C_{200} ($\Delta = 0.25$)	6.0 ± 0.2	C_{500} ($\Delta = 0.55$)	0.35 ± 0.05
C_{156}	1.2 ± 0.1	C_{400}	0.55 ± 0.05	C_{500}	0.43 ± 0.05
C_{200}	1.0 ± 0.1	C_{400} ($\Delta = 0.4$)	0.9 ± 0.1	C_{500} ($\Delta = 0.4$)	0.9 ± 0.1
C_{200} (larger)	1.6 ± 0.1	C_{400} ($\Delta = 0.3$)	2.0 ± 0.2	C_{500} ($\Delta = 0.3$)	2.3 ± 0.1

[a] Information on the system sizes is given in Table 2. The t_0 values listed here are well described by eq 8 with $K = (197 \pm 34) \times 10^3$.

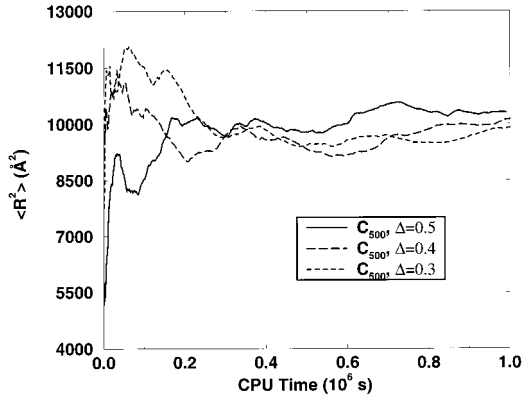

Figure 13. Running average of the mean-square end-to-end distance $\langle R^2 \rangle$ of the C_{500} PE melt with (a) $\Delta = 0.5$ (solid line), (b) $\Delta = 0.4$ (dashed line), and (c) $\Delta = 0.3$ (dotted line). The reader can immediately recognize that all three curves converge practically to the same result but with different rates, the convergence being faster for the system with the broader ($\Delta = 0.5$) chain-length distribution, in agreement with the predicted scaling of the characteristic time t_0 with Δ ($T = 450$ K and $P = 1$ atm).

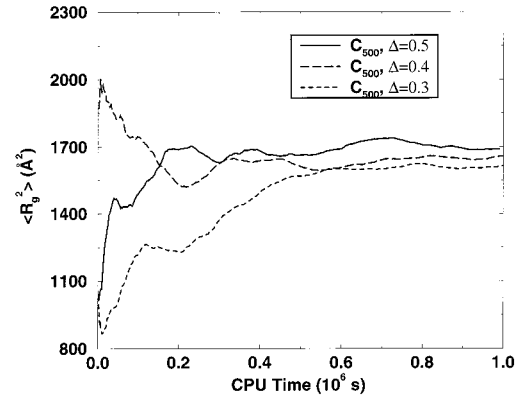

Figure 14. Running average of the mean-square radius of gyration $\langle R_g^2 \rangle$ of the C_{500} PE melt with (a) $\Delta = 0.5$ (solid line), (b) $\Delta = 0.4$ (dashed line), and (c) $\Delta = 0.3$ (dotted line). As with the mean-square end-to-end distance $\langle R^2 \rangle$, the reader can recognize that all three curves converge to the same result but with different rates, the convergence being faster for the broader chain-length distribution, again in agreement with the predicted scaling of the characteristic time t_0 with Δ ($T = 450$ K and $P = 1$ atm).

question, we have defined descriptors of the internal structure of chains and analyzed their relaxation with CPU time. The Rouse normal modes of the chains could have been chosen as such descriptors.[3] A somewhat different set of descriptors was chosen here as more representative of local conformational relaxation, given the connectivity changes induced by the EB algorithm.

We think of any chain in the system as a continuous curve in space. Let s be the contour length variable along the chain. If we scale s with the current length of the chain, then s takes values from 0 (chain start) up to 1 (chain end). We consider a sequence of discretizations of s, defined by dividing the chain into an integer number of subchains of equal contour length. Consider, for example, that we split each chain in our system into 10 successive subchains, each one of length equal to $^1/_{10}$ of the length of the entire chain. In order to probe the relaxation of the chain internal structure at a very local level, we accumulate the average time autocorrelation function of the unit vectors $\mathbf{u}_s(t)$ directed along the end-to-end vectors of all subchains of reduced length $s = {}^1/_{10}$

Table 5. Dependence of the Chain Mean-Square End-to-End Distance $\langle R^2 \rangle$, As Obtained from Bulk EB Monte Carlo Runs and from Fast Sampling of Continuous Unperturbed Chains, on the Molecular Model ($T = 450$ K and $P = 1$ atm)

	this model		Smit et al. model		Yoon et al. model	
$\bar{X}$	bulk chains	CUCs	bulk chains	CUCs	bulk chains	CUCs
C_{24}	335 ± 27	350	380 ± 25	355	310 ± 18	326
C_{78}	1490 ± 50	1497	1580 ± 100	1530	1270 ± 80	1368
C_{156}	3070 ± 150	3180		3350		2810
C_{200}	4100 ± 150	4135		4330		3760
C_{400}	8600 ± 300	8460				
C_{500}	10200 ± 400	10630				

Table 6. Dependence of the Chain Mean-Square Radius of Gyration $\langle R_g^2 \rangle$, As Obtained from Bulk EB Monte Carlo Runs and from Fast Sampling of Continuous Unperturbed Chains, on the Molecular Model ($T = 450$ K and $P = 1$ atm)

	this model		Smit et al. model		Yoon et al. model	
$\bar{X}$	bulk chains	CUCs	bulk chains	CUCs	bulk chains	CUCs
C_{24}	44 ± 1.5	43	46 ± 1.5	44	40 ± 2.0	40
C_{78}	224 ± 10	223	230 ± 28	227	190 ± 25	200
C_{156}	500 ± 18	505		514		446
C_{200}	665 ± 20	655		673		597
C_{400}	1450 ± 70	1410				
C_{500}	1650 ± 100	1770				

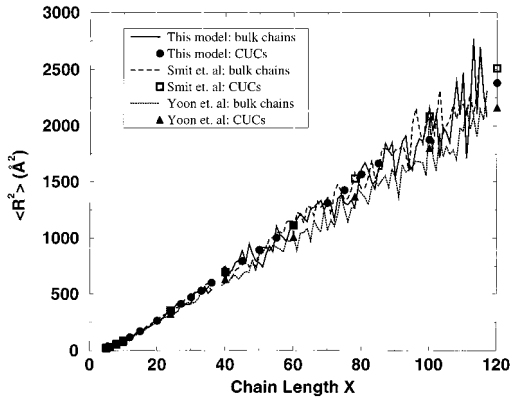

Figure 15. Chain mean-square end-to-end distance $\langle R^2 \rangle$ as a function of chain length X obtained with the three molecular models investigated in the present study. The curves track $\langle R^2 \rangle$ for bulk melt chains as obtained from C_{24} and C_{78} simulations with $\Delta = 0.5$, and the points show the same quantity for continuous unperturbed chains (CUCs). The solid curve and the filled circles correspond to the model used in the present study, the long-dashed curve and the open squares correspond to the Smit et al. model, and the dotted curve and the filled triangles correspond to the Yoon et al. model ($T = 450$ K and $P = 1$ atm).

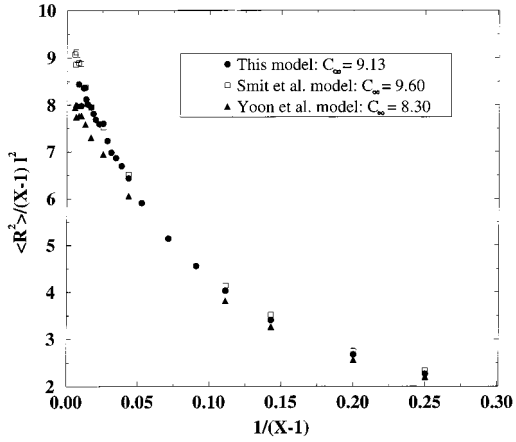

Figure 16. Dependence of the characteristic ratio C_X on the inverse number of bonds $1/(X-1)$ for unperturbed PE chains. The asymptotic limits for all models at large X are reported in the legend (T = 450 K and P = 1 atm).

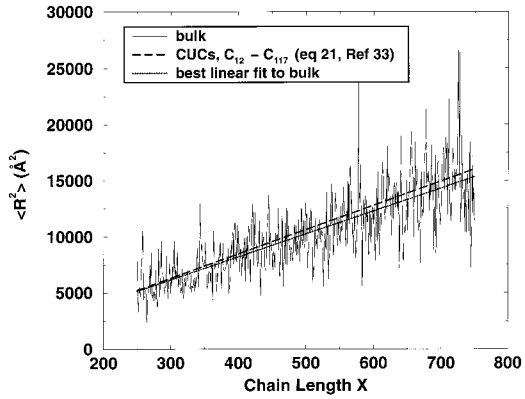

Figure 17. Chain mean-square end-to-end distance as a function of chain length. The thin solid line tracks $\langle R^2 \rangle$ for bulk melt chains, the thick dotted line represents the best linear fit to the bulk data, and the thick long-dashed line represents the prediction of the analytical equation reported in ref 33. The bulk results have been obtained from a simulation of the C_{500} chain system with a value of $\Delta = 0.5$ (T = 450 K and P = 1 atm).

throughout the simulation. We then consider the end-to-end unit vectors of all subchains of reduced length $s = {}^2/_{10}$ (each such subchain consisting of two subchains of reduced length $s = {}^1/_{10}$) and accumulate their autocorrelation function. We repeat the process for subchains of reduced length $s = {}^3/_{10}$, $s = {}^4/_{10}$, ..., $s = {}^{10}/_{10}$, with larger values of s providing information about conformational relaxation at a less local level. Clearly, in this procedure we only autocorrelate subchains that (a) belong to the same chain, (b) have the same scaled length, and (c) start at the same scaled distance from the chain start. Results obtained for $s = {}^{10}/_{10}$ reduce to the global autocorrelation functions displayed in Figure 8.

With this scheme, the contribution to the time autocorrelation functions from chain sections excised from one chain and appended to another in the course of EB moves gets smaller and smaller as these chain sections get shorter and shorter in relation to the mean chain length in the system. For small Δ and small s, the observed relaxation is governed more by the local CONROT and reptation moves and less by the global EB moves. The autocorrelation functions $\langle \mathbf{u}_s(0) \cdot \mathbf{u}_s(t) \rangle$ obtained in this way can be described satisfactorily by stretched exponential (KWW) expressions,[45,46] with the

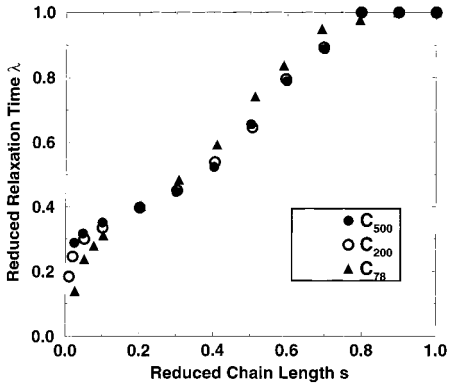

Figure 18. Relaxation of the inner parts of a chain. λ is the correlation time of the end-to-end unit vector of a subchain which represents a fraction s of the total contour of a chain, made dimensionless through division by the correlation time of the end-to-end unit vector of the entire chain. The reduced relaxation time λ is shown as a function of the reduced length s of the subchain. Filled circles correspond to the C_{500} chain system, open circles to the C_{200} chain system, and filled triangles to the C_{78} chain system (T = 450 K, P = 1 atm, and $\Delta = 0.5$).

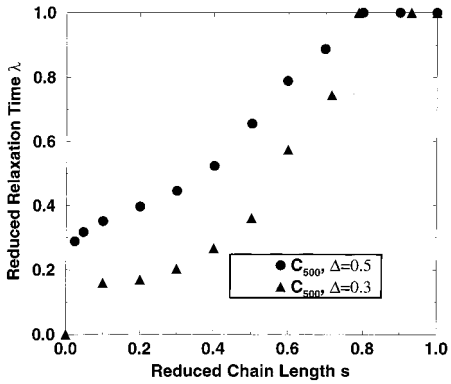

Figure 19. Relaxation of the inner parts of a chain: as in Figure 18, but for different widths Δ of the chain length distribution of a C_{500} system. Circles correspond to $\Delta = 0.5$ and triangles to $\Delta = 0.3$ (T = 450 K and P = 1 atm).

stretching exponent approaching 1 as s increases toward 1. Relaxation times, in CPU seconds, for various s values were obtained as integrals of the autocorrelation functions $\int_0^\infty \langle \mathbf{u}_s(0) \cdot \mathbf{u}_s(t) \rangle \, dt$. For each system studied, all relaxation times were reduced by the relaxation time for $s = 1$, which governs the entire end-to-end vector of chains and is commensurate with the values of t_0 listed in Table 4 and described by eq 8. Representative results for the dependence of this reduced relaxation time on the scaled subchain size are shown in Figures 18 and 19.

Figure 18 presents λ as a function of s for three systems: C_{500}, C_{200}, and C_{78}. In all these cases, $\Delta = 0.5$. Because λ is scaled with the value it attains for $s = 1$, all curves end at the point ($s = 1$, $\lambda = 1$). Apart from minor details, all three figures show the same, general behavior: The relaxation time λ first increases with increasing scaled chain segment length, reaching a plateau around $s = 0.2$. As s is increased further, λ starts rising more steeply, going through an inflection point around $\lambda \approx 1 - \Delta = 0.5$. For $s \geq 0.9$, λ stays practically constant at the value it assumes for $s = 1$. The figure clearly shows that the longest relaxation times are presented by the longest subchains. The dependence of relaxation time on subchain size is strongly nonlinear but monotonic. If conformational

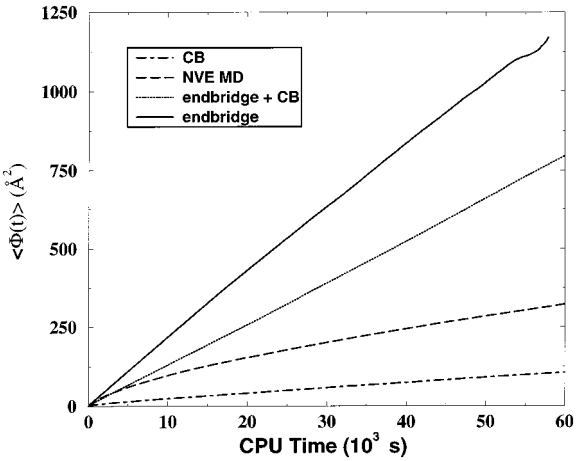

Figure 20. Segment mean-square displacement $\langle\Phi(t)\rangle$ as a function of CPU time for the "smaller" C_{78} chain system obtained with (a) the NPT configurational bias MC method (dot-dashed line), (b) the NVE MD method (dashed line), and (c) the present end-bridging MC method (solid line). Also shown is the curve obtained with the end-bridging MC method where 50% of the attempted end-bridging moves have been replaced by configurational bias moves (dotted line) ($T = 450$ K and $P = 1$ atm).

features are relaxed at the level of entire chains, the local conformation is also relaxed, at least for $\bar{X}$ up to 500. Although the EB move only induces changes in the long-range connectivity of the system, local relaxation remains quite efficient owing to the simultaneous use of the CONROT move.

It is conceivable that, for larger values of $\bar{X}$, a maximum might actually develop in the $\lambda = \lambda(s)$ curves, indicating that the most slowly relaxing conformational characteristic is no more the entire chain end-to-end vector but rather an inner, intermediate-size subchain. This possibility will be investigated in future simulations with longer-chain systems.

Figure 19 shows the function $\lambda(s)$ for the C_{500} chain system when Δ is reduced from 0.5 to 0.3. The reader should keep in mind that overall relaxation is considerably slower for the $\Delta = 0.3$ system (compare Table 4, eq 8, and associated discussion). The points for $\Delta = 0.3$ in Figure 19 appear below those for $\Delta = 0.5$ mainly because of the normalization used for λ values. Reducing Δ clearly brings a significant change in the shape of the $\lambda(s)$ curve; the relaxation rates of short and long subchains are now more disparate, and the inflection point in the $\lambda(s)$ curve moves to the vicinity of the new $1 - \Delta = 0.7$.

Additional evidence for the efficiency of the EB MC algorithm in equilibrating the local structure of the polymer can be provided by the rate with which the mean-square displacement $\langle\Phi(t)\rangle$ of segments evolves as a function of CPU time.[3,47] In defining $\langle\Phi(t)\rangle$, the three segments of a newly constructed bridge in a successful EB move assume the identities of the three segments eliminated, while all other segments maintain their identity. For the smaller C_{78} chain system, the curve $\langle\Phi(t)\rangle$ versus CPU time t is shown in Figure 20. The solid line in the figure represents the results obtained using the present EB MC algorithm with the mix of moves reported in section 4.1. The dotted curve corresponds to the results obtained when half of the EB moves are replaced by CB moves, whereas the dot-dashed curve corresponds to the results obtained when all EB moves are replaced by CB moves (compare Figure 7 and related discussion). Also shown in the figure is the curve (long-dashed) obtained from the NVE MD run. Clearly, the EB MC method is the most effective of all in displacing individual monomer units and thereby redistributing the density in the system. However, its superiority relative to the MD technique is seen to be somewhat smaller than when the comparison was made on the basis of the chain end-to-end vector autocorrelation function $\langle\mathbf{u}(t)\cdot\mathbf{u}(0)\rangle$ (see Figure 7). On the other hand, CB, without any end bridging, seems to be unable to produce any significant segment displacement during the available CPU time.

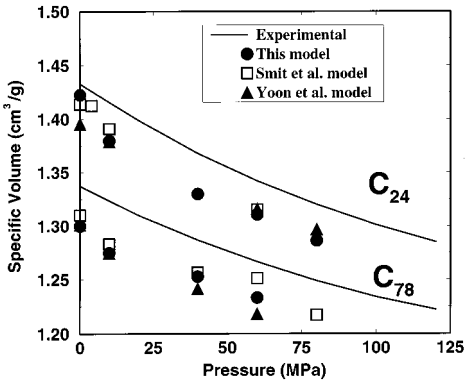

Figure 21. Dependence of the specific volume v of the C_{24} and C_{78} PE melt systems on pressure P at constant temperature $T = 450$ K, as predicted by the present study and as measured experimentally. Results obtained with all three molecular models used in this work are shown. Circles correspond to the model primarily used in the present study ("this model"), triangles to the Yoon et al. model, and squares to the Smit et al. model.

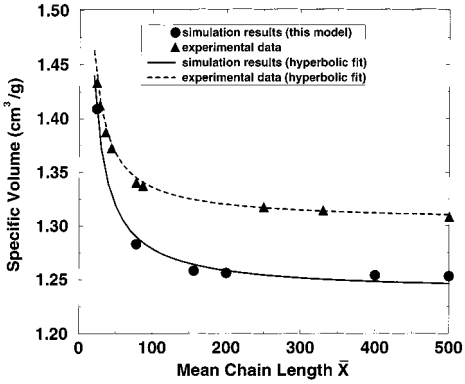

Figure 22. Dependence of the specific volume v on mean chain length $\bar{X}$, as predicted by the present EB method with the molecular model primarily used in this work ("this model") and as measured experimentally. Fits of hyperbolic functions to the predicted and experimental points according to eq 9 are also shown ($T = 450$ K and $P = 1$ atm).

5.4. Thermodynamic Properties. Specific volume (v) predictions from simulations on the systems studied in this work are shown in Figures 21 and 22. Figure 21 presents the variation of volume with pressure for the C_{24} and C_{78} PE melts, respectively, both with $\Delta = 0.5$. The figures include results for the same systems from simulations with the two other molecular models discussed in section 2. Experimental data[22,48] from monodisperse C_{24} and C_{78} melts are also shown. The figures indicate that all three models overpredict the density of the C_{24} and C_{78} melts over the entire range of pressures (1−80 atm) studied. Overall, the predictions of all three models are not very different. The isothermal compressibility $\kappa_T = -(1/v)(\partial v/\partial P)_T$, calculated from the slope of the $v(P)$ curve and from fluctuations of the

volume at constant pressure,[49] is very similar for the three models and for the two different mean molecular weights. The simulation value of $\kappa_T = 1.43 \times 10^{-9}$ Pa^{-1} agrees remarkably well with experimental measurements.[48]

Figure 22 shows the variation of the specific volume at $T = 450$ K and $P = 1$ atm with the average chain length $\bar{X}$ for the molecular model used in the present study and how it compares with experimental data. The simulation results (filled circles) have been obtained for a value of $\Delta = 0.5$; changing Δ was found to have no effect on the specific volume. Experimental results found in the literature for particular values of $\bar{X}$ are also shown in the figure as filled triangles.[22,48] As with the C_{24} and C_{78} systems, the simulation predictions overestimate the density of the PE melts over the entire regime of chain lengths studied. The figure further shows that, as $\bar{X}$ increases, v decreases monotonically. For $\bar{X} \geq 150$, however, a plateau is seen to be reached, beyond which very little variation of v with $\bar{X}$ takes place. This tendency is seen in both the simulation and the experimental data.

In the literature, the decrease of v with $\bar{X}$ is usually correlated by a relation of the form

$$v = v_\infty + v_0/\bar{X} \tag{9}$$

where v_∞ is the value of v at infinite chain length and v_0 a proportionality constant, describing the rate with which v falls with increasing $\bar{X}$. By fitting the data of Figure 22 to eq 9, the following values are obtained for the two coefficients v_∞ and v_0. From the simulation data, $v_\infty = 1.238$ cm^3/g and $v_0 = 4.037$ cm^3/g, whereas from the experimental data, $v_\infty = 1.305$ cm^3/g and $v_0 = 3.180$ cm^3/g.

The error bars in Figure 22 are small, of the same size as the symbols used to represent the data, i.e., about ± 0.005 cm^3/g. This is the result of (a) the excellent equilibration of the systems, thanks to the efficiency of the EB technique, and (b) the long duration of the runs for which results are reported in this work. On the other hand, if the run length is kept short, the error bars will increase. This is the case with the data reported in Figure 21: the simulations from which these data were collected have been run for short times, because of CPU time limitations, which resulted in somewhat higher error bars, about ± 0.008 cm^3/g.

Recently two new alkane potential parametrizations, NERD and TraPPE,[50,51] have been proposed, which give accurate predictions of densities and vapor−liquid equilibria. It is likely that these models may lead to improved volumetric properties for PE as well. Their performance will be assessed in future EB-based simulations.

5.5. Structural Properties. Having established the ability of the EB Monte Carlo method to equilibrate the long-range conformational features of long polymer chains and to capture quite satisfactorily their *PVT* behavior, we turn to the prediction of the melt structure. This is investigated by calculating the intrachain pair density function $w(r)$ and the intermolecular pair distribution function $g(r)$.[31,33]

Figure 23 shows $w(r)$ for various mean chain lengths $\bar{X}$. Polydispersity has negligible effect on $w(r)$. The first Dirac peak at small distances is due to pairs of mers separated by one bond (1.54 Å). The second Dirac peak is due to pairs of mers two bonds apart (2.55 Å), while the other sharp peaks reflect conformational preferences

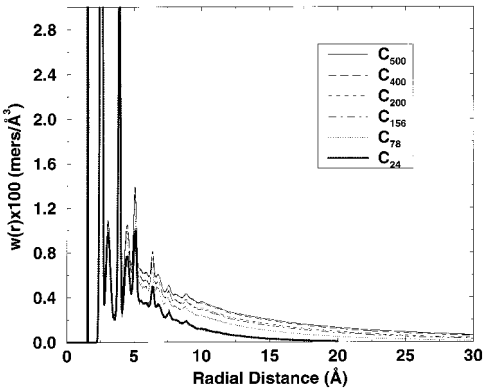

Figure 23. Intrachain pair density function $w(r)$ for all five systems studied in the present work. For comparison, the curve corresponding to a shorter (C_{24}) system is also included ($T = 450$ K and $P = 1$ atm).

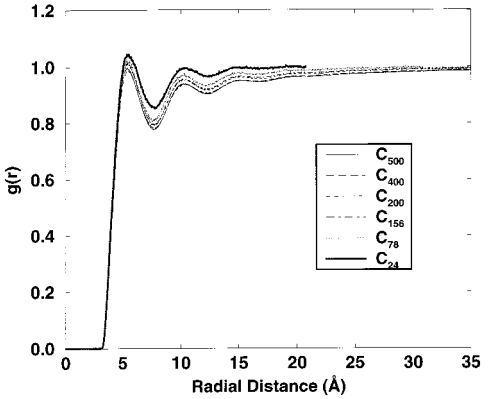

Figure 24. Intermolecular pair distribution function $g(r)$ for all five systems studied in the present work. For comparison, the curve corresponding to a shorter (C_{24}) system is also included. The simulation of this latter system was conducted in a smaller box (edge length ≈ 29 Å); this explains why the corresponding $g(r)$ extends only up to ≈21 Å ($T = 450$ K and $P = 1$ atm).

of the chains. For example, the fourth peak at about 3.92 Å is due to two mers separated by three bonds, the middle one of which is in a trans conformation, while the third peak at about 3.06 Å is due to two mers separated by three bonds, the middle one of which is in a gauche conformation. Because the locations of these peaks reflect chain-length-independent intramolecular characteristics, they are the same for all six systems shown in the figure (C_{24}, C_{78}, C_{156}, C_{200}, C_{400}, and C_{500}). Where the systems differ substantially is the overall decay of $w(r)$ with distance, which reflects the finite size of the chain segment cloud: the longer the chain, the slower the decay of $w(r)$ at larger r values.

The structure of the molten PE polymers can also be examined by calculating the intermolecular pair distribution function $g(r)$. This is shown in Figure 24 for six different mean chain lengths. The figure shows quite clearly the so-called "correlation hole effect" as well as its scaling with $\bar{X}$. At small distances compared to the radius of gyration, $g(r)$ is suppressed relative to what it would be for a monatomic fluid. This happens because the segment cloud of the chain partially excludes mers of other chains from coming close to the reference mer on the chain. Analyzing the data in Figure 24 shows that the distance over which the correlation hole effect persists scales with the square root of the chain length[52,53] and, in fact, is commensurate with the radius of gyration of the chain (compare Table 6). Local packing

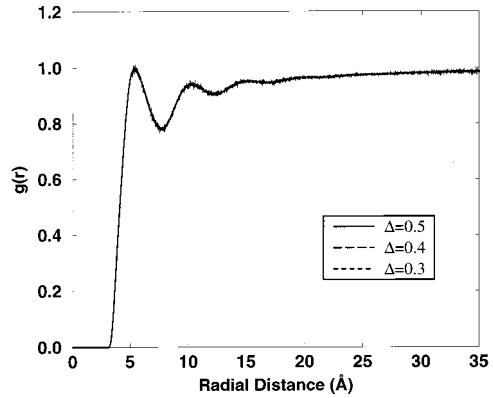

Figure 25. Intermolecular pair distribution function $g(r)$ for the C_{500} system, for different values of the reduced half-width of the chain-length distribution Δ. The curves obtained are coincident ($T = 450$ K and $P = 1$ atm).

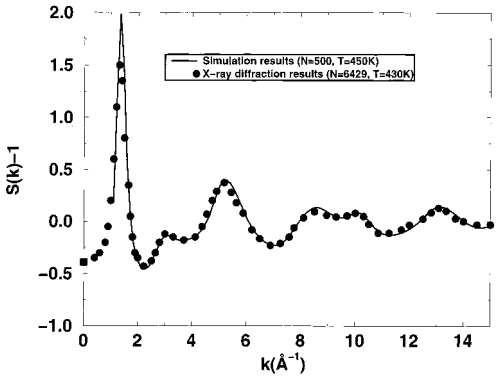

Figure 26. Simulated and experimental X-ray diffraction patterns of linear polyethylene at $T = 450$ K and $P = 1$ atm. The simulations have been carried out with the C_{500} chain system and a value of $\Delta = 0.5$. The experimental points have been taken from the measurements reported by Honnell et al.[54]

in the melt is characterized by the peaks in $g(r)$ seen at short distances. The positions of these peaks shift somewhat to the left as $\bar{X}$ increases, especially at small $\bar{X}$. This reflects the increase in density with increasing $\bar{X}$, seen most characteristically in Figure 22. Polydispersity has no effect at all on $g(r)$: for $\Delta = 0.5$, 0.4, and 0.3, the curve $g(r)$ does not change, as clearly seen in Figure 25.

By combining the intrachain pair density and the intermolecular pair distribution functions, we can form the total pair distribution function $g^{tot}(r)$:

$$g^{tot}(r) \equiv g(r) + w(r)/(n/V) \qquad (10)$$

The total pair distribution function is of great significance because its Fourier transform gives the static structure factor $S(k)$, which can be measured experimentally by X-ray diffraction studies.

$$S(k) = 1 + \rho n \int_0^\infty 4\pi r^2 \frac{\sin(kr)}{kr}[g^{tot}(r) - 1]\, dr \qquad (11)$$

$S(k)$ was seen to be very similar for all five systems studied in the present work. Thus, in Figure 26 only the $S(k)$ curve for the C_{500} system is reported (solid line). In the same figure we plot as filled circles the experimental points from X-ray diffraction measurements at 1 atm and 430 K reported by Honnell et al.[54] The agreement between the two curves is excellent. It is particularly encouraging that the first peak in $S(k)$,

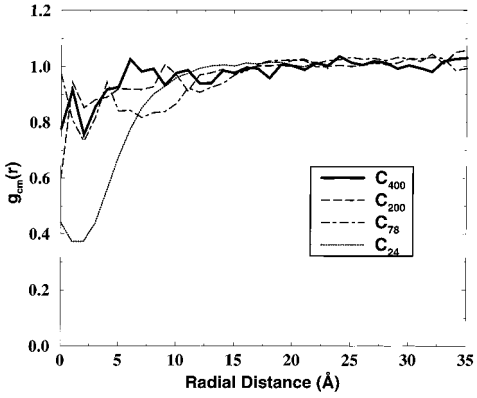

Figure 27. Chain center-of-mass pair distribution function $g_{cm}(r)$ for the C_{24}, C_{78}, C_{200}, and C_{400} chain systems. For comparison, the curve corresponding to the shorter C_{24} chain system is also included ($T = 450$ K and $P = 1$ atm).

which reflects mainly intermolecular correlations, is captured well by the simulation. The filled square at $k = 0$ marks the value $(n/V)k_BT\kappa_T - 1$, based on the simulation estimate of κ_T reported above. It is seen that this value is in excellent agreement with the experimental $S(k) - 1$ in the limit $k = 0$, as required by the compressibility theorem under conditions of thermodynamic equilibrium.[55]

Another interesting quantity, characterizing structure at the level of entire chains, is the chain center-of-mass pair distribution function, $g_{cm}(r)$. The dependence of $g_{cm}(r)$ on r and its scaling with chain length are shown in Figure 27. Results for long chains are rather noisy because of the small number of chains present in each simulation. The first point to notice in the $g_{cm}(r)$ versus r curves is the absence of strong correlations between the centers of mass; only for the shorter C_{24} chain system does a pronounced correlation hole effect appear. For the longer chain systems, $g_{cm}(r)$ seems to exhibit no particular structure, in strong contrast to the intermolecular pair distribution function for mers. A second important point to notice in Figure 27 is that, interestingly enough, $g_{cm}(0)$ assumes a nonzero value. This, although strange at first glance, is due to the fact that different chains can interpenetrate profusely, with their centers of mass coming very close without violating the nonoverlap requirement for mers. From this study of $g_{cm}(r)$ it emerges, therefore, that the "potential of mean force" $-k_BT \ln g_{cm}(r)$ between the centers of two long chains in the melt is an extremely weak and soft interaction.

6. Summary and Conclusions

A complete analysis of the geometric formulation and an efficient numerical implementation of the end-bridging MC algorithm have been presented. The unique capability of the method to equilibrate really long-chain systems efficiently has been documented by analyzing its performance on five different PE melts with mean chain lengths ranging from C_{78} up to C_{500}, significantly longer than any other system equilibrated so far by atomistic simulation.

Particular emphasis has been laid on quantifying the performance of the move. Simple analytical arguments, based on the premise that the chains and subchains involved in an end-bridging move behave as random coils, have been used to estimate the CPU time t_0 needed for the mean-square displacement of chain centers of

mass to reach the mean-square end-to-end distance of chains. These arguments have led to the conclusion that t_0 should scale as $n/(\bar{X}\Delta^{2.5})$, where n is the total number of mers, $\bar{X}$ is the average chain length, and Δ is the reduced half-width of the chain-length distribution function. The simulation findings were seen to follow this scaling exactly as long as the average chain length is greater than about C_{150} and Δ exceeds 0.5. Analysis of orientational autocorrelation functions of subchains of different contour lengths has demonstrated that local conformational features relax faster than the end-to-end vector for mean chain lengths up to 500, and thus decorrelation of the chain end-to-end vector and chain center-of-mass diffusion can safely be used as criteria for equilibration. For fixed shape of the molecular weight distribution, the performance of the move increases in proportion to the mean chain length, in sharp contrast to what happens with all other known MC moves and MD techniques.

Detailed results have been presented for the thermodynamic and structural properties of long polymer melts, as well as for their conformational distributions, using three different potential models.[33,37,38] All three models overestimate the density by ca. 4%. The Yoon et al. model[38] is in best agreement with the experimental characteristic ratio of linear PE. Simulation predictions for the chain-length dependence of the density and for the structure factor are in excellent agreement with experiment. Intensive thermodynamic properties are quite insensitive to the degree of polydispersity and show little dependence on the mean molecular weight beyond C_{150}, at which length truly "polymeric" behavior seems to set in. Future efforts will focus on the study of the dynamic properties of these equilibrated long-chain systems and on the application of the method to other systems consisting of chains bearing short or long branches along the backbone.

Acknowledgment. This work was supported by the European Commission through BRITE/Euram Project BRPR-CT96-0145. We also thank the General Secretariat for Research and Technology of Greece for partial support in the form of a PENED 95 grant, No. 218. We are grateful to Manolis Doxastakis for preparing the figures which illustrate the structural changes induced in the end-bridging move. Stimulating discussions with our BRITE project partners, and, in particular, with Professors Manolo Laso and Hans Christian Öttinger, are deeply appreciated. Also appreciated are very fruitful exchanges of ideas with Dr. Krishna Pant. We are indebted to ICE/HT-FORTH for a generous allocation of CPU time on the Origin 2000 machine.

Appendix A. Equations Specifying the Trimer Bridging Problem

This appendix presents details of the formulation leading to eq 4 describing the trimer bridging problem and sketches the strategy followed for the determination of all of its solutions.

To express $\mathbf{r}_2$ analytically in terms of ϕ_L, we define a right-handed coordinate frame $[\mathbf{u}_1, \mathbf{u}_2, \mathbf{u}_3]$, as shown in Figure 4L. In this figure, $\mathbf{r}_P$ is a projection of $\mathbf{r}_2$ onto the axis of bond 1 and $\mathbf{r}_2^0$ is a point of intersection of C_2 with the plane $(\mathbf{r}_L, \mathbf{r}_0, \mathbf{r}_1)$, corresponding to the position of $\mathbf{r}_2$ for which $\phi_L = 0$. The unit vectors $\mathbf{u}_1$ and $\mathbf{u}_2$ are directed along $\mathbf{r}_1 - \mathbf{r}_0$ and $\mathbf{r}_2^0 - \mathbf{r}_P$, respectively.

Similarly, to express $\mathbf{r}_4$ analytically in terms of ϕ_R, we define a right-handed coordinate frame $[\mathbf{v}_1, \mathbf{v}_2, \mathbf{v}_3]$, as shown in Figure 4R. Here, $\mathbf{r}_Q$ is the projection of $\mathbf{r}_4$ on the axis of bond 6, $\mathbf{r}_4^0$ is a point of intersection of C_4 with the plane $(\mathbf{r}_5, \mathbf{r}_6, \mathbf{r}_R)$, corresponding to $\phi_R = 0$, and the unit vectors $\mathbf{v}_1$ and $\mathbf{v}_2$ are directed along $\mathbf{r}_Q - \mathbf{r}_5$ and $\mathbf{r}_4^0 - \mathbf{r}_Q$, respectively.

C_3, the locus of $\mathbf{r}_3$ (Figure 5), is a circle of known radius R centered at $\mathbf{r}_N$, where $\mathbf{r}_N$ is the projection of $\mathbf{r}_3$ onto the axis connecting $\mathbf{r}_1$ and $\mathbf{r}_5$. A right-handed local coordinate frame $[\mathbf{w}_1, \mathbf{w}_2, \mathbf{w}_3]$ is defined with origin at $\mathbf{r}_N$, with $\mathbf{w}_1$ directed along $\mathbf{r}_5 - \mathbf{r}_1$ and $\mathbf{w}_2$ lying in the plane $(\mathbf{r}_1, \mathbf{r}_5, \mathbf{r}_M)$ and pointing toward $\mathbf{r}_M$.

With the above definitions, the analytical expressions for $\mathbf{r}_2$, $\mathbf{r}_3$, and $\mathbf{r}_4$ in terms of ϕ_L, ψ, and ϕ_R become

$$\mathbf{r}_2 = \mathbf{r}_P + l_2 \sin\theta_1 \cos\phi_L \mathbf{u}_2 + l_2 \sin\theta_1 \sin\phi_L \mathbf{u}_3 \quad \text{(A.1)}$$

$$\mathbf{r}_3 = \mathbf{r}_N + R\cos\psi \mathbf{w}_2 + R\sin\psi \mathbf{w}_3 \quad \text{(A.2)}$$

$$\mathbf{r}_4 = \mathbf{r}_Q + l_5 \sin\theta_5 \cos\phi_R \mathbf{v}_2 + l_5 \sin\theta_5 \sin\phi_R \mathbf{v}_3 \quad \text{(A.3)}$$

where the unit vectors $\mathbf{u}_i$, $\mathbf{w}_i$, and $\mathbf{v}_i$ (see Figures 4 and 5) are calculated from the position vectors $\mathbf{r}_L$, $\mathbf{r}_0$, $\mathbf{r}_1$, $\mathbf{r}_5$, $\mathbf{r}_6$, and $\mathbf{r}_R$ as

$$\mathbf{u}_1 = \frac{\mathbf{r}_1 - \mathbf{r}_0}{l_1} \quad \text{(A.4)}$$

$$\mathbf{u}_2 = -\frac{l_1(\mathbf{r}_L - \mathbf{r}_0)}{|(\mathbf{r}_L - \mathbf{r}_0)\times(\mathbf{r}_1 - \mathbf{r}_0)|} + \frac{(\mathbf{r}_L - \mathbf{r}_0)\cdot(\mathbf{r}_1 - \mathbf{r}_0)}{|(\mathbf{r}_L - \mathbf{r}_0)\times(\mathbf{r}_1 - \mathbf{r}_0)|}\frac{(\mathbf{r}_1 - \mathbf{r}_0)}{l_1} \quad \text{(A.5)}$$

$$\mathbf{u}_3 = -\frac{(\mathbf{r}_0 - \mathbf{r}_L)\times(\mathbf{r}_1 - \mathbf{r}_0)}{|(\mathbf{r}_0 - \mathbf{r}_L)\times(\mathbf{r}_1 - \mathbf{r}_0)|} \quad \text{(A.6)}$$

$$\mathbf{w}_1 = \frac{\mathbf{r}_5 - \mathbf{r}_1}{|\mathbf{r}_5 - \mathbf{r}_1|} \quad \text{(A.7)}$$

$$\mathbf{w}_2 = \frac{|\mathbf{r}_5 - \mathbf{r}_1|}{|(\mathbf{r}_M - \mathbf{r}_1)\times(\mathbf{r}_5 - \mathbf{r}_1)|}(\mathbf{r}_M - \mathbf{r}_1) - \frac{(\mathbf{r}_M - \mathbf{r}_1)\cdot(\mathbf{r}_5 - \mathbf{r}_1)}{|(\mathbf{r}_M - \mathbf{r}_1)\times(\mathbf{r}_5 - \mathbf{r}_1)|}\frac{(\mathbf{r}_5 - \mathbf{r}_1)}{|\mathbf{r}_5 - \mathbf{r}_1|} \quad \text{(A.8)}$$

$$\mathbf{w}_3 = \frac{(\mathbf{r}_5 - \mathbf{r}_1)\times(\mathbf{r}_M - \mathbf{r}_1)}{|(\mathbf{r}_M - \mathbf{r}_1)\times(\mathbf{r}_5 - \mathbf{r}_1)|} \quad \text{(A.9)}$$

$$\mathbf{v}_1 = -\frac{\mathbf{r}_6 - \mathbf{r}_5}{l_6} \quad \text{(A.10)}$$

$$\mathbf{v}_2 = -\frac{l_6(\mathbf{r}_R - \mathbf{r}_6)}{|(\mathbf{r}_R - \mathbf{r}_6)\times(\mathbf{r}_6 - \mathbf{r}_5)|} + \frac{(\mathbf{r}_R - \mathbf{r}_6)\cdot(\mathbf{r}_6 - \mathbf{r}_5)}{|(\mathbf{r}_R - \mathbf{r}_6)\times(\mathbf{r}_6 - \mathbf{r}_5)|}\frac{(\mathbf{r}_6 - \mathbf{r}_5)}{l_6} \quad \text{(A.11)}$$

$$\mathbf{v}_3 = -\frac{(\mathbf{r}_R - \mathbf{r}_6)\times(\mathbf{r}_6 - \mathbf{r}_5)}{|(\mathbf{r}_R - \mathbf{r}_6)\times(\mathbf{r}_6 - \mathbf{r}_5)|} \quad \text{(A.12)}$$

and the origins of the three coordinate frames are

located at

$$\mathbf{r}_P = \mathbf{r}_1 + l_2 \cos\theta_1 \frac{(\mathbf{r}_1 - \mathbf{r}_0)}{l_1} \quad \text{(A.13)}$$

$$\mathbf{r}_N = \frac{\mathbf{r}_1 + \mathbf{r}_5}{2} + \frac{\mathbf{r}_1 - \mathbf{r}_5}{2}\left(\frac{|\mathbf{r}_3 - \mathbf{r}_5|^2 - |\mathbf{r}_3 - \mathbf{r}_1|^2}{|\mathbf{r}_5 - \mathbf{r}_1|^2}\right) \quad \text{(A.14)}$$

$$\mathbf{r}_Q = \mathbf{r}_5 + l_5 \cos\theta_5 \frac{(\mathbf{r}_5 - \mathbf{r}_6)}{l_6} \quad \text{(A.15)}$$

As mentioned in the text, the reference point $\mathbf{r}_M$ is defined as

$$\mathbf{r}_M = \frac{\mathbf{r}_6 + \mathbf{r}_0}{2} \quad \text{(A.16)}$$

The radius of C_3, the locus of $\mathbf{r}_3$, is

$$R = |\mathbf{r}_3 - \mathbf{r}_1| \sqrt{1 - \left(\frac{|\mathbf{r}_5 - \mathbf{r}_1|^2 + |\mathbf{r}_3 - \mathbf{r}_1|^2 - |\mathbf{r}_5 - \mathbf{r}_3|^2}{2|\mathbf{r}_3 - \mathbf{r}_1||\mathbf{r}_5 - \mathbf{r}_1|}\right)^2} \quad \text{(A.17)}$$

where $|\mathbf{r}_3 - \mathbf{r}_1| = \sqrt{l_2^2 + l_3^2 + 2l_2 l_3 \cos\theta_2}$ and $|\mathbf{r}_5 - \mathbf{r}_3| = \sqrt{l_4^2 + l_5^2 + 2l_4 l_5 \cos\theta_4}$ have fixed values dictated by the bonding geometry.

Equations A.1−A.3 can be reduced to one equation in one unknown by applying the bond length and bond angle constraints

$$|\mathbf{r}_3 - \mathbf{r}_2|^2 = l_3^2 \quad \text{(A.18)}$$

$$|\mathbf{r}_4 - \mathbf{r}_3|^2 = l_4^2 \quad \text{(A.19)}$$

$$|\mathbf{r}_4 - \mathbf{r}_2|^2 = l_3^2 + l_4^2 + 2l_3 l_4 \cos\theta_3 \quad \text{(A.20)}$$

We define

$$a_2 = l_2 \sin\theta_1 \quad \text{(A.21)}$$

$$a_4 = l_5 \sin\theta_5 \quad \text{(A.22)}$$

Substituting eq A.1 into eq A.18 yields

$$a_L \omega_L^2 + b_L \omega_L + c_L = 0 \quad \text{(A.23)}$$

where

$$\omega_L = \tan(\phi_L/2)$$

$$a_L = (\mathbf{r}_P - \mathbf{r}_3)^2 + a_2^2 - l_3^2 - 2a_2[(\mathbf{r}_P - \mathbf{r}_3)\cdot\mathbf{u}_2]$$

$$b_L = 4a_2[(\mathbf{r}_P - \mathbf{r}_3)\cdot\mathbf{u}_3]$$

$$c_L = (\mathbf{r}_P - \mathbf{r}_3)^2 + a_2^2 - l_3^2 + 2a_2[(\mathbf{r}_P - \mathbf{r}_3)\cdot\mathbf{u}_2]$$

Equation A.23 is quadratic in ω_L. For given $\mathbf{r}_3(\psi)$, it can have two, one (degenerate), or zero real roots, depending on the sign of the discriminant $b_L^2 - 4a_L c_L$ (see Appendix B). Roots obtained through eq A.23 will be symbolized as $\phi_L(\mathbf{r}_3(\psi))$. Substitution of such a root into eq A.1 gives $\mathbf{r}_2[\phi_L(\mathbf{r}_3(\psi))] = \mathbf{r}_2(\psi)$.

Likewise, substituting eq A.3 into eq A.19 yields

$$a_R \omega_R^2 + b_R \omega_R + c_R = 0 \quad \text{(A.24)}$$

where

$$\omega_R = \tan(\phi_R/2)$$

$$a_R = (\mathbf{r}_Q - \mathbf{r}_3)^2 + a_4^2 - l_4^2 - 2a_4[(\mathbf{r}_Q - \mathbf{r}_3)\cdot\mathbf{v}_2]$$

$$b_R = 4a_4[(\mathbf{r}_Q - \mathbf{r}_3)\cdot\mathbf{v}_3]$$

$$c_R = (\mathbf{r}_Q - \mathbf{r}_3)^2 + a_4^2 - l_4^2 + 2a_4[(\mathbf{r}_Q - \mathbf{r}_3)\cdot\mathbf{v}_2]$$

Equation A.24 is quadratic in ω_R. For given $\mathbf{r}_3(\psi)$, it can have two, one (degenerate), or zero real roots, depending on the sign of the discriminant $b_R^2 - 4a_R c_R$ (see Appendix B). Solutions for ϕ_R obtained through eq A.24 will be symbolized as $\phi_R(\mathbf{r}_3(\psi))$. Substitution of such a solution into eq A.3 gives $\mathbf{r}_4[\phi_R(\mathbf{r}_3(\psi))] = \mathbf{r}_4(\psi)$.

Substituting the solution of eqs A.23 and A.24 into the third constraint eq A.20 yields the function

$$F(\psi) = |\mathbf{r}_4(\psi) - \mathbf{r}_2(\psi)|^2 - l_3^2 - l_4^2 - 2l_3 l_4 \cos\theta_3 \quad \text{(A.25)}$$

ψ is a solution to the bridging problem when $F(\psi) = 0$. In general, this function has four branches, because eq A.23 for ϕ_L and eq A.24 for ϕ_R can each contribute two real roots, for given ψ.

On the basis of the above, the following computational algorithm is adopted for seeking solutions to the trimer bridging problem which satisfy eq 4.

(A) From dimer positions and chain architecture, calculate (1) reference points $\mathbf{r}_P$, $\mathbf{r}_Q$, and $\mathbf{r}_N$, (2) local frames $[\mathbf{u}_1, \mathbf{u}_2, \mathbf{u}_3]$, $[\mathbf{v}_1, \mathbf{v}_2, \mathbf{v}_3]$, and $[\mathbf{w}_1, \mathbf{w}_2, \mathbf{w}_3]$, and (3) constants a_2 and a_4.

(B) Identify ψ domains for EB Monte Carlo feasibility (see Appendix B): (1) form fourth-order inequalities in $\tan(\psi/2)$ for the existence of ϕ_L and ϕ_R, (2) find roots of each inequality, (3) determine regions of the ψ axis in which each inequality is satisfied, (4) determine domains of the ψ axis where the two inequalities are simultaneously satisfied, and (5) determine subdomains of the feasible domains lying within the predetermined ψ wedge of width $2W$.

(C) For all four branches of $F(\psi)$, (1) perform stepwise sweeps through all feasible ψ domains, (2) identify all possible solutions of $F(\psi) = 0$, (3) for each solution ψ, calculate $\phi_L(\psi)$ and $\phi_R(\psi)$, (4) for each solution, calculate the trimer atom positions $\mathbf{r}_2(\phi_L)$, $\mathbf{r}_3(\psi)$, and $\mathbf{r}_4(\phi_R)$, and (5) store all bridging configurations.

Appendix B. Trimer Bridging Feasibility Conditions

Feasibility conditions on the trimer bridging problem can be found by analyzing the quadratic expressions for ω_L (eq A.23) and ω_R (eq A.24) of Appendix A. For eq A.23 to have real roots, the discriminant must be nonnegative:

$$16a_2^2[(\mathbf{r}_P - \mathbf{r}_3)\cdot\mathbf{u}_3]^2 - 4[(\mathbf{r}_P - \mathbf{r}_3)^2 + a_2^2 - l_3^2]^2 + 16a_2^2[(\mathbf{r}_P - \mathbf{r}_3)\cdot\mathbf{u}_2]^2 \geq 0 \quad \text{(B.1)}$$

Substituting expressions for $\mathbf{r}_P$ (eq A.13) and $\mathbf{r}_3(\psi)$ (eq A.2) into eq B.1 yields an expression of the form

$$c_4^L \omega_N^4 + c_3^L \omega_N^3 + c_2^L \omega_N^2 + c_1^L \omega_N + c_0^L \geq 0 \quad \text{(B.2)}$$

where

$$\omega_N = \tan(\psi/2) \quad \text{(B.3)}$$

$$c_0^L = -F - A \quad \text{(B.4)}$$

$$c_1^L = 2(E - C) \quad \text{(B.5)}$$

$$c_2^L = 2(A - 2B - F) \quad \text{(B.6)}$$

$$c_3^L = 2(C + E) \quad \text{(B.7)}$$

$$c_4^L = -(F + A + D) \quad \text{(B.8)}$$

and

$$A = \frac{4}{R^2}[\{(\mathbf{r}_P - \mathbf{r}_N)\cdot\mathbf{w}_2\}^2 + a_2{}^2(\mathbf{w}_2\cdot\mathbf{u}_1)^2] \quad \text{(B.9)}$$

$$B = \frac{4}{R^2}[\{(\mathbf{r}_P - \mathbf{r}_N)\cdot\mathbf{w}_3\}^2 + a_2{}^2(\mathbf{w}_3\cdot\mathbf{u}_1)^2] \quad \text{(B.10)}$$

$$C = \frac{8}{R^2}[a_2{}^2(\mathbf{w}_2\cdot\mathbf{u}_1)(\mathbf{w}_3\cdot\mathbf{u}_1) + \{(\mathbf{r}_P - \mathbf{r}_N)\cdot\mathbf{w}_2\}\{(\mathbf{r}_P - \mathbf{r}_N)\cdot\mathbf{w}_3\}] \quad \text{(B.11)}$$

$$D = \frac{4}{R^3}[\{(\mathbf{r}_P - \mathbf{r}_N)^2 + R^2\}\{(\mathbf{r}_P - \mathbf{r}_N)\cdot\mathbf{w}_2\} + 2a_2{}^2\{(\mathbf{r}_P - \mathbf{r}_N)\cdot\mathbf{u}_1\}(\mathbf{w}_2\cdot\mathbf{u}_1) - (a_2{}^2 + l_3{}^2)\{(\mathbf{r}_P - \mathbf{r}_N)\cdot\mathbf{w}_2\}] \quad \text{(B.12)}$$

$$E = \frac{4}{R^3}[\{(\mathbf{r}_P - \mathbf{r}_N)^2 + R^2\}\{(\mathbf{r}_P - \mathbf{r}_N)\cdot\mathbf{w}_3\} + 2a_2{}^2\{(\mathbf{r}_P - \mathbf{r}_N)\cdot\mathbf{u}_1\}(\mathbf{w}_3\cdot\mathbf{u}_1) - (a_2{}^2 + l_3{}^2)\{(\mathbf{r}_P - \mathbf{r}_N)\cdot\mathbf{w}_3\}] \quad \text{(B.13)}$$

$$F = \frac{1}{R^4}[\{(\mathbf{r}_P - \mathbf{r}_N)^2 + R^2\}^2 - 2(a_2{}^2 + l_3{}^2)\{(\mathbf{r}_P - \mathbf{r}_N)^2 + R^2\} + (a_2{}^2 - l_3{}^2)^2 + 4a_2{}^2\{(\mathbf{r}_P - \mathbf{r}_N)\cdot\mathbf{u}_1\}^2] \quad \text{(B.14)}$$

All constants, reference points, and reference frame unit vectors are defined in Appendix A. The constants c_i^L are functions only of the known dimer positions and the chain bonding geometry.

In exactly the same manner, analogous conditions on ψ can be found from eq A.24, based on the existence of ϕ_R. The preceding analysis is repeated with the changes in variables $\phi_L \rightarrow \phi_R$, $\mathbf{r}_P \rightarrow \mathbf{r}_Q$, $l_3 \rightarrow l_4$, $a_2 \rightarrow a_4$, and $\mathbf{u} \rightarrow \mathbf{v}$, yielding a second fourth-order inequality in ψ,

$$c_4^R\,\omega_N{}^4 + c_3^R\,\omega_N{}^3 + c_2^R\,\omega_N{}^2 + c_1^R\,\omega_N + c_0^R \geq 0 \quad \text{(B.15)}$$

where the constants are again given by expressions (B.4)−(B.14), with the noted changes in variables.

Equations B.2 and B.15 are quartic inequalities in ω_N. The quartic polynomial on the left-hand side of each has four, two, or zero real roots. For either inequality, the roots and the sign of c_4 determine domains of ψ for which the corresponding $\phi[\mathbf{r}_3(\psi)]$ exists. The resulting feasibility conditions for each inequality are summarized in Table 7.

The intersection of the feasibility regions from eqs B.2 and B.15 defines ψ domains for which the bridging problem is feasible, i.e., where the function $F(\psi)$ exists.

Table 7. Bridging Feasibility Conditions Based on a Fourth-Order Inequality in ω_N[a]

no. of real roots	root values	feasible ω_N domains ($c_4 < 0$)	feasible ω_N domains ($c_4 > 0$)
4	$\omega_N^{(1)} \leq \omega_N^{(2)} \leq \omega_N^{(3)} \leq \omega_N^{(4)}$	$\omega_N^{(1)} \leq \omega_N \leq \omega_N^{(2)}$ $\omega_N^{(3)} \leq \omega_N \leq \omega_N^{(4)}$	$-\infty \leq \omega_N \leq \omega_N^{(1)}$ $\omega_N^{(2)} \leq \omega_N \leq \omega_N^{(3)}$ $\omega_N^{(4)} \leq \omega_N \leq \infty$
2	$\omega_N^{(1)} \leq \omega_N^{(2)}$	$\omega_N^{(1)} \leq \omega_N \leq \omega_N^{(2)}$	$-\infty \leq \omega_N \leq \omega_N^{(1)}$ $\omega_N^{(2)} \leq \omega_N \leq \infty$
0	none	none	none

[a] The inequality can have 4, 2, or 0 real roots. The constant c_4 represents c_4^L or c_4^R.

Appendix C. Jacobian of the Transformation Introduced by EB Monte Carlo Moves

Like seven-bond concerted rotation (CONROT) moves,[29] trimer bridging moves entail a temporary, nonmetric-preserving, local transformation of coordinates from the Cartesian to the constraint variables. There are many ways to define the nine constraints of the bridging problem. In this work, we use one which is not only mathematically convenient but also very efficient in terms of CPU time requirements of its algorithmic implementation.

Assuming that the seven atoms involved in the move are numbered locally from 0 to 6, the positions of atoms 0, 1, 5, and 6 are specified, while those of atoms 2, 3, and 4 making up the bridge trimer are the ones sought (see Figure 2). The position of the trimer is fully specified by the Cartesian coordinates of its constituent atoms, i.e., of $\{\mathbf{r}_2, \mathbf{r}_3, \mathbf{r}_4\}$. Alternatively, the trimer can be specified by three bond lengths, three bond angles, and three dihedral angles $\{\theta_1, \phi_1, l_2, \theta_2, \phi_2, l_3, \theta_3, \phi_3, l_4\}$ or four bond lengths and five bond angles $\{l_2, l_3, l_4, l_5, \theta_1, \theta_2, \theta_3, \theta_4, \theta_5\}$ that fix its shape, size, position, and orientation with respect to the given dimers. The bond angles in conjunction with the bond lengths fix the distances between all pairs of atoms separated by two bonds, so the last constraint representation of the trimer may be replaced by $\{l_2, l_3, l_4, l_5, l_{02}, l_{13}, l_{24}, l_{35}, l_{46}\}$.

In our formulation, the following sets of coordinates are considered: (a) $\{\mathbf{r}_2, \mathbf{r}_3, \mathbf{r}_4\}$ (I), (b) $\{\theta_1, \phi_1, l_2, \theta_2, \phi_2, l_3, \theta_3, \phi_3, l_4\}$ (II), and (c) $\{l_2, l_3, l_4, l_5, l_{02}, l_{13}, l_{24}, l_{35}, l_{46}\}$ (III).

The appropriate Jacobians of transformation from one set to another are defined as

$$J_{II\rightarrow I} = \frac{\partial(\mathbf{r}_2,\mathbf{r}_3,\mathbf{r}_4)}{\partial(\theta_1,\phi_1,l_2,\theta_2,\phi_2,l_3,\theta_3,\phi_3,l_4)} = \frac{\partial(\mathbf{r}_2,\mathbf{r}_3-\mathbf{r}_2,\mathbf{r}_4-\mathbf{r}_3)}{\partial(\theta_1,\phi_1,l_2,\theta_2,\phi_2,l_3,\theta_3,\phi_3,l_4)}$$

$$= \frac{\partial(\mathbf{r}_2)}{\partial(\theta_1,\phi_1,l_2)}\cdot\frac{\partial(\mathbf{r}_3-\mathbf{r}_2)}{\partial(\theta_2,\phi_2,l_3)}\cdot\frac{\partial(\mathbf{r}_4-\mathbf{r}_3)}{\partial(\theta_3,\phi_3,l_4)}$$

$$= (l_2{}^2\sin\theta_1)(l_3{}^2\sin\theta_2)(l_4{}^2\sin\theta_3) = l_2{}^2 l_3{}^2 l_4{}^2 \sin\theta_1\sin\theta_2\sin\theta_3 \quad \text{(C.1)}$$

Note that $J_{II\rightarrow I}$ does not depend on the torsion angles ϕ.

Also

$$J_{I\rightarrow III} = \frac{\partial(l_2,l_3,l_4,l_5,l_{02},l_{13},l_{24},l_{35},l_{46})}{\partial(\mathbf{r}_2,\mathbf{r}_3,\mathbf{r}_4)}$$

$$= \partial(|\mathbf{r}_2-\mathbf{r}_1|,|\mathbf{r}_3-\mathbf{r}_2|,|\mathbf{r}_4-\mathbf{r}_3|,|\mathbf{r}_5-\mathbf{r}_4|,|\mathbf{r}_2-\mathbf{r}_0|, |\mathbf{r}_3-\mathbf{r}_1|,|\mathbf{r}_4-\mathbf{r}_2|,|\mathbf{r}_5-\mathbf{r}_3|,|\mathbf{r}_6-\mathbf{r}_4|)/\partial(\mathbf{r}_2,\mathbf{r}_3,\mathbf{r}_4) \quad \text{(C.2)}$$

The partial derivatives required in eq C.2 can be found as

$$\frac{\partial(|\mathbf{r}_i-\mathbf{r}_j|)}{\partial r_k^{\alpha}} = \begin{cases} \dfrac{(r_i - r_j)^{\alpha}}{|\mathbf{r}_i - \mathbf{r}_j|} & \text{if } k = i \\ -\dfrac{(r_i - r_j)^{\alpha}}{|\mathbf{r}_i - \mathbf{r}_j|} & \text{if } k = j \\ \mathbf{0} & \text{otherwise} \end{cases} \tag{C.3}$$

where

$$\frac{\mathbf{r}_i - \mathbf{r}_{i-1}}{|\mathbf{r}_i - \mathbf{r}_{i-1}|} = \hat{\mathbf{b}}_i \quad \text{and}$$

$$\frac{\mathbf{r}_i - \mathbf{r}_{i-2}}{|\mathbf{r}_i - \mathbf{r}_{i-2}|} = \frac{1}{l_{i-2,i}}(l_{i-1}\hat{\mathbf{b}}_{i-1} + l_i\hat{\mathbf{b}}_i)$$

with $\hat{\mathbf{b}}_i$ being the unit vector along bond i, $l_{i-2,i} = \sqrt{l_{i-1}^2+l_i^2+2l_{i-1}l_i\cos\theta_{i-1}}$, and superscript α denoting one of the three Cartesian components.

The Jacobian of transformation from set II to set III is

$$J_{\mathrm{II}\to\mathrm{III}} = J_{\mathrm{II}\to\mathrm{I}}J_{\mathrm{I}\to\mathrm{III}} \tag{C.4}$$

One can show that, up to an immaterial factor of -1,

$$J_{\mathrm{II}\to\mathrm{III}} = \frac{l_1 l_2^2 l_3^2 l_4^2 l_6 \sin\theta_1 \sin\theta_2 \sin\theta_3}{l_{02} l_{13} l_{24} l_{35} l_{46}} \frac{1}{(\mathbf{u}_6\cdot\mathbf{e}_3)} |\det(\mathbf{B})| \tag{C.5}$$

where $\mathbf{B}$ is the matrix defined in ref 29:

$$\mathbf{B} = \begin{bmatrix} (\hat{\mathbf{b}}_1\times\mathbf{r}_{51}) & (\hat{\mathbf{b}}_2\times\mathbf{r}_{52}) & (\hat{\mathbf{b}}_3\times\mathbf{r}_{53}) & (\hat{\mathbf{b}}_4\times\mathbf{r}_{54}) & \mathbf{0} \\ (\hat{\mathbf{b}}_1\times\hat{\mathbf{b}}_6)\cdot\mathbf{e}_1 & (\hat{\mathbf{b}}_2\times\hat{\mathbf{b}}_6)\cdot\mathbf{e}_1 & (\hat{\mathbf{b}}_3\times\hat{\mathbf{b}}_6)\cdot\mathbf{e}_1 & (\hat{\mathbf{b}}_4\times\hat{\mathbf{b}}_6)\cdot\mathbf{e}_1 & (\hat{\mathbf{b}}_5\times\hat{\mathbf{b}}_6)\cdot\mathbf{e}_1 \\ (\hat{\mathbf{b}}_1\times\hat{\mathbf{b}}_6)\cdot\mathbf{e}_2 & (\hat{\mathbf{b}}_2\times\hat{\mathbf{b}}_6)\cdot\mathbf{e}_2 & (\hat{\mathbf{b}}_3\times\hat{\mathbf{b}}_6)\cdot\mathbf{e}_2 & (\hat{\mathbf{b}}_4\times\hat{\mathbf{b}}_6)\cdot\mathbf{e}_2 & (\hat{\mathbf{b}}_5\times\hat{\mathbf{b}}_6)\cdot\mathbf{e}_2 \end{bmatrix} \tag{C.6}$$

and ($\mathbf{e}_1$, $\mathbf{e}_2$, $\mathbf{e}_3$) stand for the unit vectors along the axes of the laboratory frame of reference. A special case of eq C.5 has been derived and used in refs 30 and 56. Using techniques of generalized expansion of determinants, one can further show that

$$J_{\mathrm{II}\to\mathrm{III}} = \frac{l_1 l_2^2 l_3^2 l_4^2 l_6 \sin\theta_1 \sin\theta_2 \sin\theta_3}{l_{02} l_{13} l_{24} l_{35} l_{46}}$$

$$\{-l_2 l_3 l_5[(\hat{\mathbf{b}}_1\times\hat{\mathbf{b}}_2)\cdot\hat{\mathbf{b}}_3][(\hat{\mathbf{b}}_2\times\hat{\mathbf{b}}_5)\cdot\hat{\mathbf{b}}_6][(\hat{\mathbf{b}}_3\times\hat{\mathbf{b}}_4)\cdot\hat{\mathbf{b}}_5] + l_2 l_4 l_5[(\hat{\mathbf{b}}_1\times\hat{\mathbf{b}}_2)\cdot\hat{\mathbf{b}}_5][(\hat{\mathbf{b}}_2\times\hat{\mathbf{b}}_3)\cdot\hat{\mathbf{b}}_4][(\hat{\mathbf{b}}_4\times\hat{\mathbf{b}}_5)\cdot\hat{\mathbf{b}}_6] + l_3 l_4[(\hat{\mathbf{b}}_1\times\hat{\mathbf{b}}_2)\cdot\hat{\mathbf{b}}_3][l_2(\hat{\mathbf{b}}_2\times\hat{\mathbf{b}}_3)\cdot\hat{\mathbf{b}}_4 - l_5(\hat{\mathbf{b}}_3\times\hat{\mathbf{b}}_4)\cdot\hat{\mathbf{b}}_5][(\hat{\mathbf{b}}_4\times\hat{\mathbf{b}}_5)\cdot\hat{\mathbf{b}}_6] + l_2 l_4^2[(\hat{\mathbf{b}}_1\times\hat{\mathbf{b}}_2)\cdot\hat{\mathbf{b}}_4][(\hat{\mathbf{b}}_2\times\hat{\mathbf{b}}_3)\cdot\hat{\mathbf{b}}_4][(\hat{\mathbf{b}}_4\times\hat{\mathbf{b}}_5)\cdot\hat{\mathbf{b}}_6] - l_3^2 l_5[(\hat{\mathbf{b}}_1\times\hat{\mathbf{b}}_2)\cdot\hat{\mathbf{b}}_3][(\hat{\mathbf{b}}_3\times\hat{\mathbf{b}}_4)\cdot\hat{\mathbf{b}}_5][(\hat{\mathbf{b}}_3\times\hat{\mathbf{b}}_5)\cdot\hat{\mathbf{b}}_6]\} \tag{C.7}$$

In an EB move, the coordinates in set III are independent (chosen at will from prescribed bond length and bond angle distributions), while the coordinates in sets I and II are not independent. Therefore, the appropriate Jacobian of transformation which we should use in the acceptance criteria to sample the space spanned by the Cartesian coordinates (classical flexible model of Gō and Scheraga,[40] which can be taken to the limit of infinite force constants) is $J_{\mathrm{III}\to\mathrm{I}}$. From eq C.4 we have

$$J_{\mathrm{III}\to\mathrm{I}} = \frac{1}{J_{\mathrm{I}\to\mathrm{III}}} = \frac{J_{\mathrm{II}\to\mathrm{I}}}{J_{\mathrm{II}\to\mathrm{III}}} \tag{C.8}$$

where $J_{\mathrm{II}\to\mathrm{III}}$ is taken from eq C.7 and $J_{\mathrm{II}\to\mathrm{I}}$ from eq C.1. Note that $J_{\mathrm{III}\to\mathrm{I}}$ can be used in a flexible bond length and/or flexible bond angle model.

Appendix D. Scaling of CPU Requirements for End-Bridging MC with System Size, Mean Chain Length, and Polydispersity

Let us consider the geometric problem of end bridging (see, for example, Figure 1) and label as 1 the attacking chain and as 2 the victim chain, part of which will be appended to chain 1. Let us also assume that the two chains consist of X_1 and X_2 mers, respectively, and that the part of chain 2 which will be appended to chain 1 contains X_2^{b} mers. After the move is completed, chain 1 has become 1′ and consists of $X_1 + X_2^{\mathrm{b}}$ mers; chain 2 has become 2′ and consists of $X_2^{\mathrm{a}} = X_2 - X_2^{\mathrm{b}}$ mers. We want to analyze the mean-square displacement of the centers of mass of chains 1 and 2 brought about by a successful end-bridging move.

The displacement of the center of mass of chain 1 is

$$\mathbf{r}'_{\mathrm{cm},1} - \mathbf{r}_{\mathrm{cm},1} = \frac{X_1\mathbf{r}_{\mathrm{cm},1} + X_2^{\mathrm{b}}\mathbf{r}^{\mathrm{b}}_{\mathrm{cm},2}}{X_1 + X_2^{\mathrm{b}}} - \mathbf{r}_{\mathrm{cm},1} = \frac{X_2^{\mathrm{b}}}{X_1 + X_2^{\mathrm{b}}}(\mathbf{r}^{\mathrm{b}}_{\mathrm{cm},2} - \mathbf{r}_{\mathrm{cm},1}) \tag{D.1}$$

while the displacement of the center of mass of chain 2 is

$$\mathbf{r}'_{\mathrm{cm},2} - \mathbf{r}_{\mathrm{cm},2} = \mathbf{r}^{\mathrm{a}}_{\mathrm{cm},2} - \frac{X_2^{\mathrm{a}}\mathbf{r}^{\mathrm{a}}_{\mathrm{cm},2} + X_2^{\mathrm{b}}\mathbf{r}^{\mathrm{b}}_{\mathrm{cm},2}}{X_2^{\mathrm{a}} + X_2^{\mathrm{b}}} = \frac{X_2^{\mathrm{b}}}{X_2^{\mathrm{a}} + X_2^{\mathrm{b}}}(\mathbf{r}^{\mathrm{a}}_{\mathrm{cm},2} - \mathbf{r}^{\mathrm{b}}_{\mathrm{cm},2}) \tag{D.2}$$

From eqs D.1−D.2, the mean-square displacement of the centers of mass of the two chains participating in a single successful EB move, averaged over all configurations, is

$$\langle(\mathbf{r}'_{\mathrm{cm},1} - \mathbf{r}_{\mathrm{cm},1})^2\rangle_{\mathrm{EB}} + \langle(\mathbf{r}'_{\mathrm{cm},2} - \mathbf{r}_{\mathrm{cm},2})^2\rangle_{\mathrm{EB}} = \left\langle\left(\frac{X_2^{\mathrm{b}}}{X_1 + X_2^{\mathrm{b}}}\right)^2(\mathbf{r}^{\mathrm{b}}_{\mathrm{cm},2} - \mathbf{r}_{\mathrm{cm},1})^2 + \left(\frac{X_2^{\mathrm{b}}}{X_2^{\mathrm{a}} + X_2^{\mathrm{b}}}\right)^2(\mathbf{r}^{\mathrm{a}}_{\mathrm{cm},2} - \mathbf{r}^{\mathrm{b}}_{\mathrm{cm},2})^2\right\rangle_{\mathrm{EB}} \tag{D.3}$$

The process of calculating the average in eq D.3 can be broken into two parts. The first involves calculating the average over all configurations at given X_1, X_2^{a}, and X_2^{b} and the second involves calculating the average over all X_1, X_2^{a}, and X_2^{b}.

(1) For given X_1, X_2^{a}, and X_2^{b}, for the purposes of a scaling argument, we consider chains 1 and 2^{b} as random coils. The root-mean-square distance between their centers of mass can then be approximated by the sum of their root-mean-square radii of gyration, $R_{\mathrm{g},1}$ and $R^{\mathrm{b}}_{\mathrm{g},2}$. In turn, this can be expressed in terms of the numbers of mers, bond lengths, and infinite chain-length characteristic ratio as follows:

Table 8. Values of the Quantity $S(\bar{X},\Delta)$ Defined in the Text, Eq D.7, Tabulated as a Function of $\bar{X}$ and Δ[a]

system	$S(\bar{X},\Delta)$	system	$S(\bar{X},\Delta)$	system	$S(\bar{X},\Delta)$
C_{78} (smaller)	21.3 ± 0.1	C_{200} ($\Delta = 0.375$)	32.0 ± 0.1	C_{500} ($\Delta = 0.6$)	198.5 ± 0.2
C_{78}	21.3 ± 0.1	C_{200} ($\Delta = 0.25$)	14.8 ± 0.1	C_{500} ($\Delta = 0.55$)	166.8 ± 0.2
C_{156}	42.4 ± 0.1	C_{400}	111.0 ± 0.1	C_{500}	139.0 ± 0.1
C_{200}	54.7 ± 0.1	C_{400} ($\Delta = 0.4$)	73.7 ± 0.1	C_{500} ($\Delta = 0.4$)	91.9 ± 0.1
C_{200} (larger)	54.9 ± 0.1	C_{400} ($\Delta = 0.3$)	42.5 ± 0.1	C_{500} ($\Delta = 0.3$)	53.7 ± 0.1

[a] Wherever the value of Δ is not explicitly indicated, $\Delta = 0.5$. Information on the system sizes is given in Table 2.

$$\langle(\mathbf{r}^{b}_{cm,2} - \mathbf{r}_{cm,1})^2\rangle_{EB} \approx \langle(R^{b}_{g,2} + R_{g,1})^2\rangle_{EB} \approx \frac{C_\infty}{6} l^2 \langle[(X_2^b)^{1/2} + X_1^{1/2}]^2\rangle_{EB} \quad \text{(D.4)}$$

Similarly, assuming that chain 2[a] is also long enough to behave as an unperturbed random coil,

$$\langle(\mathbf{r}^{a}_{cm,2} - \mathbf{r}^{b}_{cm,2})^2\rangle_{EB} \approx \langle(R^{a}_{g,2} + R^{b}_{g,2})^2\rangle_{EB} \approx \frac{C_\infty}{6} l^2 \langle[(X_2^a)^{1/2} + (X_2^b)^{1/2}]^2\rangle_{EB} \quad \text{(D.5)}$$

Therefore, from eqs D.3−D.5,

$$\langle(\mathbf{r}'_{cm,1} - \mathbf{r}_{cm,1})^2\rangle_{EB} + \langle(\mathbf{r}'_{cm,2} - \mathbf{r}_{cm,2})^2\rangle_{EB} \approx \frac{C_\infty}{6} l^2 \left\langle (X_2^b)^2 \left\{ \frac{[(X_2^b)^{1/2} + (X_1)^{1/2}]^2}{(X_1 + X_2^b)^2} + \frac{[(X_2 - X_2^b)^{1/2} + (X_2^b)^{1/2}]^2}{(X_2)^2} \right\} \right\rangle_{EB} = S(\bar{X},\Delta) l^2 \frac{C_\infty}{6} \quad \text{(D.6)}$$

where

$$S(\bar{X},\Delta) \equiv \left\langle (X_2^b)^2 \left\{ \frac{[(X_2^b)^{1/2} + (X_1)^{1/2}]^2}{(X_1 + X_2^b)^2} + \frac{[(X_2 - X_2^b)^{1/2} + (X_2^b)^{1/2}]^2}{(X_2)^2} \right\} \right\rangle_{EB} \quad \text{(D.7)}$$

The average on the right-hand side of eq D.7 depends on the molecular weight distribution of the melt and on the probability distribution of points of successful end bridging along the contour of the victim chain. For the flat chain-length distribution used here, assuming, as above, that 1, 2[a], and 2[b] are long enough to behave as random coils and also assuming no significant positional correlations between chain ends in the model system, this average depends only on the mean chain length $\bar{X}$ and the reduced half-width Δ of the chain-length distribution function and is therefore symbolized by $S(\bar{X},\Delta)$.

The value of $S(\bar{X},\Delta)$ can be obtained by Monte Carlo averaging. Alternatively, use can be made of the analytical distribution function $\rho(X_1,X_2,X_2^b)$,

$$\rho(X_1,X_2,X_2^b) = \begin{cases} \dfrac{1}{4\Delta\bar{X}^2 A(X_1,X_2)} & \text{if } (1-\Delta)\bar{X} \le X_1 + X_2^b \le (1+\Delta)\bar{X} \text{ and} \\ & (1-\Delta)\bar{X} \le X_2 - X_2^b \le (1+\Delta)\bar{X} \\ 0, & \text{otherwise} \end{cases} \quad \text{(D.8)}$$

with $A(X_1,X_2) \equiv \min((1+\Delta)\bar{X} - X_1, X_2 - (1-\Delta)\bar{X})$, for the chain lengths before and after a successful end-bridging move, with the integrals arising in the final expression for the average in eq D.7 being calculated numerically through Gaussian quadrature. Both approaches give exactly the same results, which are reported in Table 8. To an excellent approximation, $S(\bar{X},\Delta)$ can be described by the following equation:

$$S(\bar{X},\Delta) = 1.1\bar{X}\Delta^2 \quad \text{(D.9)}$$

The scaling with respect to $\bar{X}$ is exact, whereas that with respect to Δ is approximate, with Δ^2 being the leading term. This can be proven from eqs D.7 and D.8 if the three chain lengths X_1, X_2, and X_2^b are reduced by the average chain length $\bar{X}$ and Taylor expansions are used to deal with the square roots, whenever necessary.

According to the above arguments, the mean chain center-of-mass displacement realized in a single successful end-bridging move, averaged over all chains, is then proportional to

$$\langle[\mathbf{r}_{cm}(t) - \mathbf{r}_{cm}(0)]^2\rangle_{EB} \simeq \frac{S(\bar{X},\Delta)\frac{C_\infty}{6} l^2 + \left(\frac{n}{\bar{X}} - 2\right)0}{\frac{n}{\bar{X}}} \quad \text{(D.10)}$$

because only two of the $n/\bar{X}$ chains change in such a move.

To estimate the efficiency of EB, we further assume (a) similar mass density for all systems considered (and, therefore, dependence of the acceptance rate only on local packing), (b) equal frequency f_{EB} of attempting end-bridging moves (i.e., equal number of attempted end-bridging moves per total number of attempted moves), and (c) negligible effect of all types of moves other than end-bridging on the center-of-mass displacement of chains (i.e., end bridging is almost exclusively responsible for the long-range motion of chains). All of these assumptions are supported directly by our simulation findings. Then the mean-square displacement of chain centers of mass $\langle(\mathbf{r}_{cm}(t) - \mathbf{r}_{cm}(0))^2\rangle$ after a large number of attempted moves in the simulation will be proportional to

$$\langle(\mathbf{r}_{cm}(t) - \mathbf{r}_{cm}(0))^2\rangle \simeq N_{MC} f_{EB} p_{acc} \frac{S(\bar{X},\Delta)\frac{C_\infty}{6} l^2 + \left(\frac{n}{\bar{X}} - 2\right)0}{\frac{n}{\bar{X}}} = N_{MC} f_{EB} p_{acc} S(\bar{X},\Delta) \frac{C_\infty}{6} l^2 \frac{\bar{X}}{n} \quad \text{(D.11)}$$

where N_{MC} is the total number of attempted MC moves in the simulation and p_{acc} the acceptance rate of end-bridging moves.

The acceptance rate p_{acc} of end-bridging moves is, in general, expected to be proportional to (a) a packing-dependent numerical constant, (b) the intermolecular

end segment radial distribution function $g^{\text{inter}}_{\text{end-mer}}$ at bridging distance r_{bridging}, and (c) the probability that X_2^a and $X_1 + X_2^b$ are acceptable chain lengths. Although these three factors can be analyzed in more detail, for the purposes of the present analysis it suffices to note that, according to Table 3, p_{acc} (a) does not show any dependence on the average chain length and (b) decreases with Δ as $\Delta^{0.5}$. Thus, we can safely write down that

$$p_{\text{acc}} \approx p_0(2\Delta)^{0.5} \tag{D.12}$$

where p_0 denotes the acceptance rate for $\Delta = 0.5$ ($\approx$0.0009, i.e., a constant of the method).

As already pointed out in the main text, a MC move takes the same amount of CPU time, regardless of system size, at least for the chain lengths investigated in the present work; we have denoted this time by τ. Then, from eqs D.11 and D.12, the mean-square displacement of chain centers of mass per CPU time $t = N_{\text{MC}}\tau$ consumed is

$$\frac{\langle[\mathbf{r}_{\text{cm}}(t) - \mathbf{r}(0)]^2\rangle}{t} = \frac{f_{\text{EB}}}{\tau} p_0 \Delta^{0.5} S(\bar{X},\Delta) \frac{C_\infty}{6}\sqrt{2} l^2 \frac{\bar{X}}{n} \tag{D.13}$$

This permits calculation of the CPU time t_0 required for the mean-square displacement of chain centers of mass to become equal to the equilibrium chain end-to-end distance $\langle R^2\rangle$ as

$$t_0 = \frac{\langle R^2\rangle}{\langle[\mathbf{r}_{\text{cm}}(t) - \mathbf{r}_{\text{cm}}(0)]^2\rangle/t} \approx \frac{C_\infty \bar{X} l^2}{\frac{f_{\text{EB}}}{\tau} p_0 \Delta^{0.5} S(\bar{X},\Delta) \frac{C_\infty}{6}\sqrt{2} l^2 \frac{\bar{X}}{n}} \approx \frac{6}{\sqrt{2}} \tau \frac{1}{f_{\text{EB}}} \frac{n}{p_0} \frac{1}{\Delta^{0.5} S(\bar{X},\Delta)} \tag{D.14}$$

i.e.

$$t_0 \propto \tau \frac{n}{f_{\text{EB}} p_0 \bar{X} \Delta^{2.5}} \tag{D.15}$$

which is eq 8 of the main text.

References and Notes

(1) Flory, P. J. *Statistical Mechanics of Chain Molecules*; Interscience: New York, 1969.
(2) Curtiss, C. F.; Bird, R. B. *J. Chem. Phys.* **1981**, *74*, 2016 and 2026.
(3) Doi, M.; Edwards, S. F. *The Theory of Polymer Dynamics*; Clarendon: Oxford, U.K., 1986.
(4) Bird; R. B.; Armstrong, R. C.; Hassager, O.; Curtiss, C. F. *Dynamics of Polymeric Liquids*, Vol. 1; *Fluid Mechanics*, Vol. 2; *Kinetic Theory*, 2nd ed.; Wiley: New York, 1987.
(5) Chandler, D. *Introduction to Modern Statistical Mechanics*; Oxford University Press: New York, 1987.
(6) Allen, M. P.; Tildesley, D. J. *Computer Simulation of Liquids*; Oxford University Press: Oxford, U.K., 1987.
(7) Roe, R.-J., Ed. *Computer Simulation of Polymers*; Prentice-Hall: Englewood Cliffs, NJ, 1991.
(8) Colbourn, E. A., Ed. *Computer Simulation of Polymers*; Longman: Essex, U.K., 1994.
(9) Mattice, W. L.; Suter, U. W. *Conformational Theory of Large Molecules*; Wiley: New York, 1994.
(10) Monnerie, L. M.; Suter, U. W. Atomistic Modeling of Physical Properties. *Adv. Polym. Sci.* **1994**, *116*.
(11) Binder, K., Ed. *Monte Carlo and Molecular Dynamics Simulations in Polymer Science*; Oxford University Press: New York, 1995.
(12) Frenkel, D.; Smit, B. *Undestanding Molecular Simulation: From Algorithms to Applications*; Academic Press: New York, 1996.
(13) Weber, T. A.; Helfand, E. *J. Chem. Phys.* **1979**, *71*, 4760.
(14) Rigby, D.; Roe, R.-J. *J. Chem. Phys.* **1987**, *87*, 7285.
(15) Vacatello, M.; Avitabile, G.; Corradini, P.; Tuzi, A. *J. Chem. Phys.* **1980**, *73*, 548.
(16) Theodorou, D. N.; Suter, U. W. *Macromolecules* **1985**, *18*, 1467.
(17) Rigby, D.; Roe, R.-J. In *Computer Simulation of Polymers*; Roe, R.-J., Ed.; Prentice-Hall: Englewood Cliffs, NJ, 1991; p 79.
(18) Smith, G. D.; Yoon, D. Y. *J. Chem. Phys.* **1994**, *100*, 649. Smith, G. D.; Yoon, D. Y.; Zhu, W.; Ediger, M. D. *Macromolecules* **1994**, *27*, 5563.
(19) Mondell, M.; Grest, G. S. *J. Chem. Phys.* **1995**, *103*, 7156.
(20) Boyd, R. H. *Macromolecules* **1989**, *22*, 2477. Boyd, R. H.; Pant, P. V. K. *Macromolecules* **1991**, *24*, 4078. Boyd, R. H.; Gee, R. H.; Han, J.; Jin, Y. *J. Chem. Phys.* **1994**, *101*, 788. Jin, Y.; Pernice, M.; Boyd, R. H. *Comput. Theor. Polym. Sci.* **1996**, *6*, 9.
(21) Hutnik, M.; Argon, A. S.; Suter, U. W. *Macromolecules* **1993**, *26*, 1097.
(22) Pearson, D. S.; Ver Strate, G.; von Meerwall, E.; Schilling, F. C. *Macromolecules* **1987**, *20*, 1133.
(23) Pearson, D. S.; Fetters, L. J.; Ver Strate, G.; von Meerwall, E. *Macromolecules* **1994**, *27*, 711.
(24) These relaxation times have been estimated from the data for the diffusivity D reported in refs 22 and 23. To calculate the longest relaxation time τ_1 from D values, we have used the equation $\tau_1 = 2\langle R_g^2\rangle/\pi^2 D$ where $\langle R_g^2\rangle$ is the mean-square radius of gyration of the melt. If one uses the data for the zero-shear rate viscosity η_0 reported in refs 22 and 23 to calculate the longest relaxation time, the estimated values for τ_1 are larger by a factor of almost 2.
(25) Paul, W.; Smith, G. D.; Yoon, D. Y. *Macromolecules* **1997**, *30*, 7772. Smith, G. D.; Paul, W.; Yoon, D. Y.; Zirkel, A.; Hendricks, J.; Richter, D.; Schober, H. *J. Chem. Phys.* **1997**, *107*, 4751.
(26) de Pablo, J. J.; Laso, M.; Suter, W. U. *J. Chem. Phys.* **1992**, *96*, 2395.
(27) Siepmann, J. I.; Frenkel, D. *Mol. Phys.* **1992**, *75*, 59.
(28) Leontidis, E.; de Pablo, J. J.; Laso, M.; Suter, U. W. *Adv. Polym. Sci.* **1994**, *116*, 283. Leontidis, E.; Forrest, B. M.; Widmann, A. H.; Suter, U. W. *J. Chem. Soc., Faraday Trans.* **1995**, *91*, 2355.
(29) Dodd, L. R.; Boone, T. D.; Theodorou, D. N. *Mol. Phys.* **1993**, *78*, 961.
(30) Pant, P. V. K.; Theodorou, D. N. *Macromolecules* **1995**, *28*, 7224.
(31) Dodd, L. R.; Theodorou, D. N. *Adv. Polym. Sci.* **1994**, *116*, 249.
(32) Flory, P. J. *Principles of Polymer Chemistry*; Cornell University Press: Ithaca, NY, 1953.
(33) Mavrantzas, V. G.; Theodorou, D. N. *Macromolecules* **1998**, *31*, 6310.
(34) Harmandaris, V.; Mavrantzas, V. G.; Theodorou, D. N. *Macromolecules* **1998**, *31*, 7934.
(35) Van der Ploeg, P.; Berendsen, H. J. C. *J. Chem. Phys.* **1982**, *76*, 3271.
(36) Ryckaert, J. P.; Bellemans, A. *Chem. Phys. Lett.* **1975**, *30*, 123.
(37) Smit, B.; Karaborni, S.; Siepmann, J. I. *J. Chem. Phys.* **1995**, *102*, 2126.
(38) Paul, W.; Yoon, D. Y.; Smith, G. D. *J. Chem. Phys.* **1995**, *103*, 1702.
(39) Dahlquist, G.; Bjoerck, Å. *Numerical Methods*; Prentice-Hall: Englewood Cliffs, NJ, 1969.
(40) Gō, N.; Scheraga, H. A. *Macromolecules* **1976**, *9*, 535.
(41) Spyriouni, T.; Economou, I. G.; Theodorou, D. N. *Macromolecules* **1997**, *30*, 4744.
(42) Smith, G. D.; Yoon, D. Y.; Jaffe, R. L.; Colby, R. H.; Krishnamoorti, R.; Fetters, L. J. *Macromolecules* **1996**, *29*, 3462.
(43) Horton, J. C.; Squires, G. L.; Boothroyd, A. T.; Fetters, L. J.; Rennie, R. J.; Glinka, C. J.; Robinson, R. A. *Macromolecules* **1989**, *22*, 681.
(44) Fetters, L. J.; Graessley, W. W.; Krishnamoorti, R.; Lohse, D. J. *Macromolecules* **1997**, *30*, 4973.
(45) Williams, G.; Watts, D. C. *Trans. Faraday Soc.* **1970**, *66*, 80.

(46) Matsuoka, S. *Relaxation Phenomena in Polymers*; Hanser Publishers: Munich, 1992.
(47) Kremer, K.; Grest, G. S. *J. Chem. Phys.* **1990**, *92*, 5057; **1991**, *94*, 4103 (erratum).
(48) Dee, G. T.; Ougizawa, T.; Walsh, D. J. *Polymer* **1992**, *33*, 3462.
(49) Antoniadis, S.; Samara, C.; Theodorou, D. N. *Macromolecules* **1998**, *31*, 7944.
(50) Nath, S. K.; Escobedo, F. A.; de Pablo, J. J. *J. Chem. Phys.* **1998**, *108*, 9905.
(51) Martin, M. C.; Siepmann, J. I. *J. Phys. Chem. B* **1998**, *102*, 2569.
(52) Schweizer, K. S.; Curro, J. G. *Phys. Rev. Lett.* **1987**, *58*, 246.
(53) Curro, J. G.; Schweizer, K. S. *Macromolecules* **1987**, *20*, 1928.
(54) Honnell, K. J.; McCoy, J. D.; Curro, J. G.; Schweizer, K. S.; Narten, A. H.; Habenschuss, A. *J. Chem. Phys.* **1991**, *94*, 4659.
(55) Hansen, J.-P.; McDonald, I. *Theory of Simple Liquids*, 2nd ed.; Academic: New York, 1986.
(56) Boone, T. D. Prediction of Glass-Melt Behavior and Penetrant Sorption in Vinyl Polymers via Molecular Simulations. Ph.D. Thesis, University of California, Berkeley, Berkeley, CA, 1995.

MA981745G